JOURNAL OF COMPUTATIONAL PHYSICS **139,** 209–241 (1998)
ARTICLE NO. CP975850

A Semi-Implicit Semispectral Primitive Equation Model for Lake Circulation Dynamics and Its Stability Performance

Yongqi Wang and Kolumban Hutter

Department of Mechanics, Darmstadt University of Technology, Hochschulstr. 1, D-64289 Darmstadt, Germany
E-mail: wang@mechanik.th-darmstadt.de, hutter@mechanik.th-darmstadt.de

Received December 18, 1996; revised September 18, 1997

Key Words: semi-implicit; semispectral; stability; convergence; lake circulation; limnology; oscillation.

We present a three-dimensional numerical model for the shallow water equations, suitable for determining the wind driven currents in homogeneous and stratified lakes. The model is based on the semispectral primitive equation model (SPEM) originally developed by Haidvogel *et al.*; however, because of the relatively small water depths of inland lakes in comparison to the ocean, the explicit integration technique, employed in SPEM, requires excessively small time steps which lead to very long integration times. In this paper a semi-implicit temporal integration scheme is proposed with the aid of which time integrations through realistic time spans for inland lakes become economical. By means of a large number of test runs in which the time step, the mesh size, and the austausch coefficients are changed and the numerical stability and the convergence performances of the code are determined. Moreover, the new semi-implicit SPEM is tested as to whether it is now capable to predict or reproduce physically relevant processes that are commonly observed by physical limnologists. To this end, computational results for a homogeneous and stratified rectangle and Lake Constance are presented.

1. INTRODUCTION

Usual numerical techniques for the integration of the shallow water equations in the Boussinesq approximation make use of finite difference (FD) and finite element (FE) discretizations for the velocity, temperature, and tracer concentration fields. The vertical direction is generally distinct from the horizontal directions; i.e., the lake or ocean region is partitioned into horizontal layers with exchange processes accordingly accounted for

0021-9991/98 $25.00

between the layers; and in the horizontal directions FD- or FE-approximations are used. This a priori distinction of the vertical direction is physically motivated and lies in the geometry, aspect ratios, and natural stratification thus established by the solar radiation. However, such a layer construction leads to a piecewise constant approximation of the field variables with depth and necessarily requires a large number of layers and the selection of very thin layers in the metalimnion (generally smaller than 1 m). Methods which use in the vertical a spectral functional expansion of the field variables, but which may still employ FD- or FE-approximations in the horizontal are advantageous because of their enhanced smoothness properties.

The semispectral primitive equation model (SPEM) of Haidvogel, Wilkin and Young [23] uses Chebyshev polynomials in the vertical and FD-discretizations with central differences of a staggered Arakawa grid in the horizontal directions. Apart from the uniform resolution in the vertical, the spectral methods generally enjoy faster convergence and smaller numerical diffusion than the FD methods. Furthermore, the "order of the approximate model" (i.e., the number of functions employed in the spectral representation) is constant in shallow regions, since the number of approximating functions remains the same. Since SPEM employs the σ-transformation prior to the implementation of the discretization, the water depth in the entire lake is mapped onto the interval $[-1, 1]$, implying that the locations of the discretization points are optimally chosen for each water depth.

Classical FD approximations of the shallow water equations use a Cartesian mesh in physical space and thus lead close to the shore inavoidably to relatively poor approximations of the field variables. In SPEM this disadvantage is removed by mapping via series of Schwarz–Chrystoffel transformations a polygonal representation of the closed shoreline onto a rectangle in the computational (ξ, η)-plane. A coordinate net in this plane represents in the horizontal plane of the physical space a curvilinear orthogonal net of irregular mesh sizes. A closed polygonal shore line can always be mapped onto a rectangle; practically, however, extremely fine resolutions might be necessary to this end. In such cases a more homogeneous distribution of mesh sizes is achieved by declaring certain regions to land points. We shall encounter such a chase when considering Lake Constance.

In oceanographic applications SPEM has proved to be very reliable and very successful; e.g. [4, 6–8, 12, 13, 22, 23, 25, 30–32, 54, 69, 71]. An important disadvantage of SPEM, which does not show in oceanographical problems or is at most of peripheral significance but crucial in limnological applications, is the explicit discretization of the time-derivatives of the field variables with all consequences of the size of the time step Δt. Because explicit schemes are only conditionally stable, this explicit time step must be restricted by the minimal spatial mesh size. When 3D FD-approximations are used, this is the smallest layer thickness Δz, which in the thermocline depth of lakes may only be one or a few meters, thus necessitating extremely small time steps, if numerical instabilities are to be avoided. In SPEM, the analogue of the layer thickness is the number of spectral functions, N, called the *order* of the model. It follows that it is impossible to integrate over limnologically relevant times, i.e., approximately 1 month. For Lake Constance, for instance, with a resolution of $(L \times M) \times N = (65 \times 17) \times 12$ mesh points and Chebyshev polynomials the maximal time step guaranteeing stable integration is $\Delta t = 1.5$ s. This dilemma points at the purpose of this paper: To introduce a semi-implicit scheme for the integration in time to enhance numerical stability and reduce computational expenditures for integration over limnologically relevent times (i.e., approximately 1 month).

In Section 2 we outline the model in the Boussinesq-approximated shallow water equations, briefly explain the original SPEM integration technique and point at its peculiarities when explicit procedures in the temporal integration are used. We turn in Section 3 to a method of semi-implicit integration in time, in which the horizontal directions are consistently treated as explicit while the vertical direction is treated implicitly. The method yields a considerably more stable scheme than the fully explicit one.

Once this is recognized, we analyse in Section 4 the numerical properties of the semi-implicit scheme in comparison with the original explicit temporal integration. To delimit its stability range, we vary the austausch coefficients, time-steps, spatial mesh sizes, and order of the spectral expansion, and we tabulate its performance properties. In Section 5 the convergence properties are analyzed. In Section 6 we finally illustrate the model performance by demonstrating results obtained from a realistic barotropic and baroclinic circulation problem, respectively.

2. THE MODEL

2.1. *Field Equations*

The governing equations describing the thermodynamics of lake circulation processes driven by wind and solar radiation are the balance laws of mass, momentum, and energy complemented by a thermal equation of state and turbulent closure conditions for the Reynolds stresses and the heat flux, in which diffusivities of momentum and heat are taken to account for the anisotropy effects of the turbulent intensity; different values apply in the horizontal and vertical directions. When imposing the Boussinesq assumption and the shallow-water assumption through an appropriate scaling, the field equations reduce to the following simplified equation set:

$$
\begin{aligned}
&\frac{\partial u}{\partial x}+\frac{\partial v}{\partial y}+\frac{\partial w}{\partial z}=0,\\
&\frac{\partial u}{\partial t}+\boldsymbol{v}\cdot\operatorname{grad}u-fv=-\frac{\partial\phi}{\partial x}+\frac{\partial}{\partial x}\left(\nu_H\frac{\partial u}{\partial x}\right)+\frac{\partial}{\partial y}\left(\nu_H\frac{\partial u}{\partial y}\right)+\frac{\partial}{\partial z}\left(\nu_V\frac{\partial u}{\partial z}\right),\\
&\frac{\partial v}{\partial t}+\boldsymbol{v}\cdot\operatorname{grad}v+fu=-\frac{\partial\phi}{\partial y}+\frac{\partial}{\partial x}\left(\nu_H\frac{\partial v}{\partial x}\right)+\frac{\partial}{\partial y}\left(\nu_H\frac{\partial v}{\partial y}\right)+\frac{\partial}{\partial z}\left(\nu_V\frac{\partial v}{\partial z}\right),\\
&0=-\frac{\partial\phi}{\partial z}-\frac{\rho g}{\rho_0},\\
&\rho=\rho(T),\\
&\frac{\partial T}{\partial t}+\boldsymbol{v}\cdot\operatorname{grad}T=\frac{\partial}{\partial x}\left(D_H^T\frac{\partial T}{\partial x}\right)+\frac{\partial}{\partial y}\left(D_H^T\frac{\partial T}{\partial y}\right)+\frac{\partial}{\partial z}\left(D_V^T\frac{\partial T}{\partial z}\right)
\end{aligned}
\tag{1}
$$

of balance of mass, now requiring the solenoidicity of the velocity field, momentum, in which the vertical balance reduces to the hydrostatic pressure balance, the equation of state, and the energy balance for the temperature evolution. In Eqs. (1), $\boldsymbol{v}=(u, v, w)$; f, ρ, ρ_0, ϕ, T are, respectively, the velocity vector, Coriolis parameter, density, reference density, dynamic pressure ($\phi=p/\rho_0$, p is pressure), temperature. Furthermore, ν_H, ν_V are horizontal and vertical momentum; D_H^T, D_V^T are horizontal and vertical heat diffusivities.

As for boundary conditions, the rigid lid assumption is applied at the free surface and the flow is tangential to the bed. Furthermore, it will be assumed that no heat flows across the free or basal surfaces and that wind is transmitted through the free surface by prescribing the surface shear tractions. Similarly, basal shear tractions obey a viscous sliding law. Applying the "rigid lid assumption" at the free surface eliminates from the solution high speed surface-gravity waves. Thus the influence of the motion of the free surface is ignored in the vertically integrated mass balance. This amounts to assuming the volume transport is solenoidal and to making it derivable from a streamfunction that can be determined independently of the baroclinic response.

2.2. *A Brief Description of the Original SPEM*

SPEM employs a curvilinear coordinate system that follows both a polygonal shore line and the bottom topography. Variable bottom topography is implemented by the following so-called σ-transformation

$$(x, y, z) \mapsto \hat{x} = x, \quad \hat{y} = y, \quad \sigma = 1 + 2\frac{z}{h(x, y)}, \tag{2}$$

where $h(x, y)$ describes the bathymetry, σ varies from -1 at the bottom $z = -h(x, y)$ to $+1$ at the (underformed) free surface $z = 0$. This transformation allows the expansion of all field variables into an orthogonal function set (here the Chebyshev polynomials). In addition, by using the Schwarz–Chrystoffel transformation the interior of the polygonal horizontal lake domain is mapped onto a rectangle in the (ξ, η) domain

$$\left.\begin{aligned} x &= \hat{x}(\xi, \eta) \\ y &= \hat{y}(\xi, \eta) \end{aligned}\right\} \Longleftrightarrow \begin{cases} \xi = \hat{\xi}(x, y), \\ \eta = \hat{\eta}(x, y). \end{cases} \tag{3}$$

In this orthogonal curvilinear coordinate system the vectorial arc length increment $d\boldsymbol{s}$ is given by

$$d\boldsymbol{s} = \frac{d\xi}{m}\hat{\boldsymbol{e}}_\xi + \frac{d\eta}{n}\hat{\boldsymbol{e}}_\eta, \tag{4}$$

where $\hat{\boldsymbol{e}}_\xi, \hat{\boldsymbol{e}}_\eta$ are unit vectors pointing into the ξ- and η-directions, respectively; m^2, n^2 are the diagonal elements of the contravariant metric tensor belonging to (3).

After implementing the transformations (2) and (3) the lake volume domain is mapped onto a cube. In the coordinates ξ, η, σ the governing differential equations (1) take the forms

$$\begin{aligned} &\frac{\partial}{\partial t}\left(\frac{hu}{mn}\right) + \frac{\partial}{\partial \xi}\left(\frac{hu^2}{n}\right) + \frac{\partial}{\partial \eta}\left(\frac{huv}{m}\right) + \frac{\partial}{\partial \sigma}\left(\frac{hu\Omega}{mn}\right) \\ &\quad - \left\{\left(\frac{f}{mn}\right) + v\frac{\partial}{\partial \xi}\left(\frac{1}{n}\right) - u\frac{\partial}{\partial \eta}\left(\frac{1}{m}\right)\right\} hv \\ &\quad = -\left\{\left(\frac{h}{n}\right)\frac{\partial \phi}{\partial \xi} - (1-\sigma)\left(\frac{gh\rho}{2\rho_0 n}\right)\frac{\partial h}{\partial \xi}\right\} + \mathcal{F}_u, \end{aligned} \tag{5}$$

$$\frac{\partial}{\partial t}\left(\frac{hv}{mn}\right)+\frac{\partial}{\partial \xi}\left(\frac{huv}{n}\right)+\frac{\partial}{\partial \eta}\left(\frac{hv^2}{m}\right)+\frac{\partial}{\partial \sigma}\left(\frac{hv\Omega}{mn}\right)$$
$$+\left\{\left(\frac{f}{mn}\right)+v\frac{\partial}{\partial \xi}\left(\frac{1}{n}\right)-u\frac{\partial}{\partial \eta}\left(\frac{1}{m}\right)\right\}hu \tag{6}$$
$$=-\left\{\left(\frac{h}{m}\right)\frac{\partial \phi}{\partial \eta}-(1-\sigma)\left(\frac{gh\rho}{2\rho_0 m}\right)\frac{\partial h}{\partial \eta}\right\}+\mathcal{F}_v,$$

$$\frac{\partial}{\partial t}\left(\frac{hT}{mn}\right)+\frac{\partial}{\partial \xi}\left(\frac{huT}{n}\right)+\frac{\partial}{\partial \eta}\left(\frac{hvT}{m}\right)+\frac{\partial}{\partial \sigma}\left(\frac{h\Omega T}{mn}\right)=\mathcal{D}_T, \tag{7}$$

$$\rho=\rho(T,p), \tag{8}$$

$$\frac{\partial \phi}{\partial \sigma}=-\left(\frac{gh\rho}{2\rho_0}\right), \tag{9}$$

$$\frac{\partial}{\partial \xi}\left(\frac{hu}{n}\right)+\frac{\partial}{\partial \eta}\left(\frac{hv}{m}\right)+\frac{\partial}{\partial \sigma}\left(\frac{h\Omega}{mn}\right)=0, \tag{10}$$

in which, u, v are the horizontal physical components in the ξ- and η-directions of the velocity field. Then

$$\Omega(\xi,\eta,\sigma,t)=\frac{1}{h}\left[(1-\sigma)mu\frac{\partial h}{\partial \xi}+(1-\sigma)nv\frac{\partial h}{\partial \eta}+2w\right] \tag{11}$$

is the vertical component of the velocity field in the σ transformed coordinates. Furthermore, the frictional and the diffusive terms $\mathcal{F}_u, \mathcal{F}_v, \mathcal{D}_T$ are given by

$$\mathcal{F}_u=\frac{\partial}{\partial \xi}\left(\frac{\nu_H mh}{n}\frac{\partial u}{\partial \xi}\right)+\frac{\partial}{\partial \eta}\left(\frac{\nu_H nh}{m}\frac{\partial u}{\partial \eta}\right)+\frac{\partial}{\partial \sigma}\left(\frac{4\nu_V}{hmn}\frac{\partial u}{\partial \sigma}\right), \tag{12}$$

$$\mathcal{F}_v=\frac{\partial}{\partial \xi}\left(\frac{\nu_H mh}{n}\frac{\partial v}{\partial \xi}\right)+\frac{\partial}{\partial \eta}\left(\frac{\nu_H nh}{m}\frac{\partial v}{\partial \eta}\right)+\frac{\partial}{\partial \sigma}\left(\frac{4\nu_V}{hmn}\frac{\partial v}{\partial \sigma}\right), \tag{13}$$

$$\mathcal{D}_T=\frac{\partial}{\partial \xi}\left(\frac{D_H^T mh}{n}\frac{\partial T}{\partial \xi}\right)+\frac{\partial}{\partial \eta}\left(\frac{D_H^T nh}{m}\frac{\partial T}{\partial \eta}\right)+\frac{\partial}{\partial \sigma}\left(\frac{4D_V^T}{hmn}\frac{\partial T}{\partial \sigma}\right), \tag{14}$$

respectively (see [23]). In these equations the kinematic, ν_H, ν_V, and the thermal, D_H^T, D_V^T, diffusivities are to be treated as functions of space (and time).

In SPEM all field variables, in which the vertically integrated flow has been eliminated, are expanded as

$$b(\xi,\eta,\sigma,t)=\sum_{k=0}^{N}P_k(\sigma)\hat{b}_k(\xi,\eta,t), \tag{15}$$

in which $P_k(\sigma)$ are modified Chebyshev polynomials, and the summation index N denotes the order of the expansion, the number of "modes" by which the function $b(\xi,\eta,\sigma,t)$ is approximated. In SPEM it is not the coefficient functions $\hat{b}_k(\xi,\eta,t)$ that are determined,

but the field variable itself,

$$b_n = \sum_{k=0}^{N} P_k(\sigma_n)\hat{b}_k, \quad n = 0, 1, 2, \ldots, N, \tag{16}$$

in which the number of selected collocation points is larger by one than the order N of the expansion (15). In vector–matrix notation Eq. (16) takes the form

$$\boldsymbol{b} = \boldsymbol{F}\hat{\boldsymbol{b}} \quad \text{or} \quad \hat{\boldsymbol{b}} = \boldsymbol{F}^{-1}\boldsymbol{b}. \tag{17}$$

$\boldsymbol{F}^{-1}$ exists if the locations σ_n are properly selected. If, moreover,

$$R_{nk} = \frac{\partial P_k(\sigma_n)}{\partial \sigma}, \quad S_{nk} = \int_{\sigma_n}^{1} P_k(\sigma)\, d\sigma, \tag{18}$$

then differentiation and integration with respect to σ can be performed with the polynomials; i.e.,

$$\frac{\partial \boldsymbol{b}}{\partial \sigma} \hat{=} \delta_\sigma \boldsymbol{b} = \boldsymbol{R}\boldsymbol{F}^{-1}\boldsymbol{b} := \boldsymbol{C}_{DZ}\boldsymbol{b}, \tag{19}$$

$$\left(\int_{-1}^{1} b\, d\sigma, \int_{\sigma_1}^{1} b\, d\sigma, \ldots, \int_{\sigma_N}^{1} b\, d\sigma\right)^T \hat{=} I_\sigma^1 \boldsymbol{b} = \boldsymbol{S}\hat{\boldsymbol{b}} = \boldsymbol{S}F^{-1}b := \boldsymbol{C}_{INT}\boldsymbol{b}. \tag{20}$$

$\boldsymbol{C}_{DZ}$ and $\boldsymbol{C}_{INT}$ are matrices which are known, once the polynomials have been selected.

Finite differentiations in the horizontal are represented according to an Arakawa C-mesh; thus,

$$\frac{\partial b}{\partial \xi} \hat{=} \delta_\xi b = \frac{b_{i+1/2,\,j} - b_{i-1/2,\,j}}{\triangle \xi}, \quad \frac{\partial b}{\partial \eta} \hat{=} \delta_\eta b = \frac{b_{i,\,j+1/2} - b_{i,\,j-1/2}}{\triangle \eta}. \tag{21}$$

If averages over the spatial increments $\Delta\xi$ and $\Delta\eta$ are denoted by $\overline{(\,)}^{\xi}$ and $\overline{(\,)}^{\eta}$, respectively, then

$$\overline{b_{i,\,j}}^{\xi} = \frac{b_{i+1/2,\,j} + b_{i-1/2,\,j}}{2}, \quad \overline{b_{i,\,j}}^{\eta} = \frac{b_{i,\,j+1/2} + b_{i,\,j-1/2}}{2}.$$

The indices i, j denote the numberings in the horizontal. In the following we will use these notations. The discretized versions of Eqs. (5)–(10) are given in [23].

3. IMPLICIT INTEGRATION IN TIME

Most field equations derived above possess the form

$$\frac{\partial \Phi(t)}{\partial t} = \mathcal{F}(\Phi, t). \tag{22}$$

In a leap frog procedure it takes the form

$$\Phi(t + \triangle t) = \Phi(t - \triangle t) + 2\Delta t \mathcal{F}(t) \tag{23}$$

and can explicitly be solved for $\Phi(t+\Delta t)$ if the fields at all nodal points i, j, k are known at times $t-\Delta t$ and t. Because such explicit integrations are conditionally stable the spatial mesh size dictates the time step Δt for stable integration. The smallest layer thickness Δz is the limiting discretization step; in SPEM it corresponds to the order N of the spectral expansion. As already mentioned, this severely delimits the time spans over which the equations can be integrated. They are usually smaller than physically relevant time spans. For Lake Constance the needed maximum Δt is 1.5 s, if the spatial resolution is $(L \times M) \times N = (65 \times 17) \times 12$.

This situation requires that implicit, i.e., unconditionally stable schemes or semi-implicit, i.e., improved conditionally stable schemes be employed. For multidimensional systems ADI-schemes are a possible avenue for the latter case [68]. Test computations showed that for typical lake circulation problems, i.e., distinct shallowness of the basins the stability performance of a numerical scheme that only uses implicit temporal integration in the σ-direction is even better than the ADI-method. This means that the instability of the explicit scheme is primarily to the vertical direction, since the smallest nodal point distance in the vertical is very much smaller than a corresponding minimal distance between two nodal points in the horizontal. Furthermore, the computational expenditures for the ADI-method are much larger than for an implicit temporal integration only in the vertical direction [68]. For this reason computations presented below will be performed with an implicit time integration only in the vertical direction.

For the time step $(t^n \to t^{n+1})$, implicit in the σ-direction, but explicit in the ξ- and η-directions, the equations read:

momentum equation in ξ-direction

$$\begin{aligned}
&\frac{\overline{h}^{\xi}}{\overline{m}^{\xi}\overline{n}^{\xi}}\left(\frac{u^{n+1}-u^{n-1}}{2\Delta t}\right)+\delta_{\xi}\left\{\overline{u^{n}}^{\xi}\overline{\left(\frac{u^{n}\overline{h}^{\xi}}{\overline{n}^{\xi}}\right)}^{\xi}\right\}+\delta_{\eta}\left\{\overline{u^{n}}^{\eta}\overline{\left(\frac{v^{n}\overline{h}^{\eta}}{\overline{m}^{\eta}}\right)}^{\xi}\right\}\\
&\quad+\delta_{\sigma}\left\{u^{n+1}\frac{\overline{h}^{\xi}\overline{\Omega^{n}}^{\xi}}{\overline{m}^{\xi}\overline{n}^{\xi}}\right\}-\overline{\left\{\frac{f}{mn}+\overline{v^{n}}^{\eta}\delta_{\xi}\left(\frac{1}{n}\right)-\overline{u^{n}}^{\xi}\delta_{\eta}\left(\frac{1}{m}\right)\right\}h\overline{v^{n}}^{\eta}}^{\xi}\\
&=-\frac{\overline{h}^{\xi}}{\overline{n}^{\xi}}\delta_{\xi}\phi^{n}+(1-\sigma)\frac{g\overline{h}^{\xi}\overline{\rho^{n}}^{\xi}}{2\rho_{0}\overline{n}^{\xi}}\delta_{\xi}h+\delta_{\xi}\left(\frac{\nu_{H}mh}{n}\delta_{\xi}u^{n}\right)\\
&\quad+\delta_{\eta}\left(\frac{\overline{\nu_{H}}^{\xi\eta}\overline{n}^{\xi\eta}\overline{h}^{\xi\eta}}{\overline{m}^{\xi\eta}}\delta_{\eta}u^{n}\right)+\delta_{\sigma}\left(\frac{4\overline{\nu_{V}}^{\xi}}{\overline{h}^{\xi}\overline{m}^{\xi}\overline{n}^{\xi}}\delta_{\sigma}u^{n+1}\right),
\end{aligned}\tag{24}$$

momentum equation in η-direction

$$\begin{aligned}
&\frac{\overline{h}^{\eta}}{\overline{m}^{\eta}\overline{n}^{\eta}}\left(\frac{v^{n+1}-v^{n-1}}{2\Delta t}\right)+\delta_{\xi}\left\{\overline{v^{n}}^{\xi}\overline{\left(\frac{u^{n}\overline{h}^{\xi}}{\overline{n}^{\xi}}\right)}^{\eta}\right\}+\delta_{\eta}\left\{\overline{v^{n}}^{\eta}\overline{\left(\frac{v^{n}\overline{h}^{\eta}}{\overline{m}^{\eta}}\right)}^{\eta}\right\}\\
&\quad+\delta_{\sigma}\left\{\frac{v^{n+1}\overline{h}^{\eta}\overline{\Omega^{n}}^{\eta}}{\overline{m}^{\eta}\overline{n}^{\eta}}\right\}-\overline{\left\{\frac{f}{mn}+\overline{v^{n}}^{\eta}\delta_{\xi}\left(\frac{1}{n}\right)-\overline{u^{n}}^{\xi}\delta_{\eta}\left(\frac{1}{m}\right)\right\}hu^{n}}^{\eta}
\end{aligned}$$

$$= -\frac{\overline{h}^{\eta}}{\overline{m}^{\eta}}\delta_\eta \phi^n + (1-\sigma)\frac{g\overline{h}^{\eta}\overline{\rho^n}^{\eta}}{2\rho_0\overline{m}^{\xi}}\delta_\eta h + \delta_\xi\left(\frac{\overline{\nu_H}^{\xi\eta}\overline{m}^{\xi\eta}\overline{h}^{\xi\eta}}{\overline{n}^{\xi\eta}}\delta_\xi v^n\right) \tag{25}$$

$$+ \delta_\eta\left(\frac{\nu_H n h}{m}\delta_\eta v^n\right) + \delta_\sigma\left(\frac{4\overline{\nu_V}^{\eta}}{\overline{h}^{\eta}\overline{m}^{\eta}\overline{n}^{\eta}}\delta_\sigma v^{n+1}\right),$$

temperature equation

$$\frac{h}{mn}\left(\frac{T^{n+1}-T^{n-1}}{2\Delta t}\right) + \delta_\xi\left\{\frac{u^n\overline{h}^{\xi}\overline{T^n}^{\xi}}{\overline{n}^{\xi}}\right\} + \delta_\eta\left\{\frac{v^n\overline{h}^{\eta}\overline{T^n}^{\eta}}{\overline{m}^{\eta}}\right\} + \delta_\sigma\left\{\frac{h\Omega^n T^{n+1}}{mn}\right\} \tag{26}$$

$$= \delta_\xi\left(\frac{\overline{D_H^T}^{\xi}\overline{m}^{\xi}\overline{h}^{\xi}}{\overline{n}^{\xi}}\delta_\xi T^n\right) + \delta_\eta\left(\frac{\overline{D_H^T}^{\eta}\overline{n}^{\eta}\overline{h}^{\eta}}{\overline{m}^{\eta}}\delta_\eta T^n\right) + \delta_\sigma\left(\frac{4D_V^T}{hmn}\delta_\sigma T^{n+1}\right).$$

This discretization is chosen such that at the new time level only linear equations emerge and that pressure terms remain explicit. This avoids coupling of equations which are uncoupled in their differential form; see [68].

Because a spectral expansion is used in the vertical direction, the vertical derivatives are not expressed in terms of finite differences and the system of equations governing is not tridiagonal as in semi-implicit schemes of finite differences. This is clear from (19); the derivative of a field variable with respect to σ is exclusively expressed by a matrix $\boldsymbol{C}_{DZ}$ which only depends on the properties of the Chebyshev polynomials that premultiplies the vector of field quantities evaluated at the vertical nodal points. For instance, the vertical advective acceleration in (24) reads

$$\frac{\overline{h}^{\xi}}{\overline{m}^{\xi}\overline{n}^{\xi}}\delta_\sigma\begin{pmatrix} u^{n+1}_{i,j,0}\overline{\Omega^n_{i,j,0}}^{\xi} \\ u^{n+1}_{i,j,1}\overline{\Omega^n_{i,j,1}}^{\xi} \\ \vdots \\ u^{n+1}_{i,j,N}\overline{\Omega^n_{i,j,N}}^{\xi}\end{pmatrix} = \frac{\overline{h}^{\xi}}{\overline{m}^{\xi}\overline{n}^{\xi}}\boldsymbol{C}_{DZ}\begin{pmatrix} u^{n+1}_{i,j,0}\overline{\Omega^n_{i,j,0}}^{\xi} \\ u^{n+1}_{i,j,1}\overline{\Omega^n_{i,j,1}}^{\xi} \\ \vdots \\ u^{n+1}_{i,j,N}\overline{\Omega^n_{i,j,N}}^{\xi}\end{pmatrix}. \tag{27}$$

If second-order differentiations with respect to σ are involved, the boundary conditions at the free surface and the base must be incorporated after the performance of the first differentiation, and the second differentiation should be performed afterwards.

As an example, consider the vertical austausch term in the momentum equation in the ξ-direction, Eq. (24). In a first step, the matrix $\boldsymbol{C}_{DZ}$ is subdivided into the block matrices

$$\boldsymbol{C}_{DZ} = (\boldsymbol{C}_{DZa}, \boldsymbol{C}_{DZb}, \boldsymbol{C}_{DZc}) = \begin{pmatrix}\boldsymbol{C}_{DZ\alpha} \\ \boldsymbol{C}_{DZ\beta} \\ \boldsymbol{C}_{DZ\gamma}\end{pmatrix}, \tag{28}$$

in which $\boldsymbol{C}_{DZ}, \boldsymbol{C}_{DZa}, \boldsymbol{C}_{DZb}, \boldsymbol{C}_{DZc}, \boldsymbol{C}_{DZ\alpha}, \boldsymbol{C}_{DZ\beta}$, and $\boldsymbol{C}_{DZ\gamma}$ represent, respectively, $(N+1)\times(N+1)$, $(N+1)\times 1$, $(N+1)\times(N-1)$, $(N+1)\times 1$, $1\times(N+1)$, $(N-1)\times(N+1)$, and $1\times(N+1)$ matrices which all are known. For $i = \text{const}$, $j = \text{const}$, the vertical derivative

at all vertical nodal lines are represented as

$$\begin{aligned}\frac{4\overline{\nu_V}^{\xi}}{\overline{h}^{\xi}\overline{m}^{\xi}\overline{n}^{\xi}}\delta_\sigma \boldsymbol{u}_{i,j}^{n+1} &= \frac{4\overline{\nu_V}^{\xi}}{\overline{h}^{\xi}\overline{m}^{\xi}\overline{n}^{\xi}}\boldsymbol{C}_{DZ}\boldsymbol{u}_{i,j}^{n+1} \\ &= \frac{4\overline{\nu_V}^{\xi}}{\overline{h}^{\xi}\overline{m}^{\xi}\overline{n}^{\xi}}\begin{pmatrix}\boldsymbol{C}_{DZ\alpha}\boldsymbol{u}_{i,j}^{n+1}\\ \boldsymbol{C}_{DZ\beta}\boldsymbol{u}_{i,j}^{n+1}\\ \boldsymbol{C}_{DZ\gamma}\boldsymbol{u}_{i,j}^{n+1}\end{pmatrix} = \frac{2}{\overline{m}^{\xi}\overline{n}^{\xi}}\begin{pmatrix}\frac{2\overline{\nu_{V_{i,j,0}}}^{\xi}}{\overline{h}^{\xi}}\boldsymbol{C}_{DZ\alpha}\boldsymbol{u}_{i,j}^{n+1}\\ \frac{2\overline{\nu_V}^{\xi}}{\overline{h}^{\xi}}\boldsymbol{C}_{DZ\beta}\boldsymbol{u}_{i,j}^{n+1}\\ \frac{2\overline{\nu_{V_{i,j,N}}}^{\xi}}{\overline{h}^{\xi}}\boldsymbol{C}_{DZ\gamma}\boldsymbol{u}_{i,j}^{n+1}\end{pmatrix},\end{aligned} \tag{29}$$

where $\boldsymbol{u}_{i,j}^{n+1} = (u_{i,j,0}^{n+1}, u_{i,j,1}^{n+1}, \ldots, u_{i,j,N}^{n+1})^T$.

Next, the dynamical boundary conditions at the free surface and at the bottom are incorporated as

$$\frac{4\overline{\nu_V}^{\xi}}{\overline{h}^{\xi}\overline{m}^{\xi}\overline{n}^{\xi}}\delta_\sigma \boldsymbol{u}_{i,j}^{n+1} = \frac{2}{\overline{m}^{\xi}\overline{n}^{\xi}}\begin{pmatrix}\frac{1}{\rho_0}\tau_{\xi i,j}^{h}\\ \frac{2\overline{\nu_V}^{\xi}}{\overline{h}^{\xi}}\boldsymbol{C}_{DZ\beta}\boldsymbol{u}_{i,j}^{n+1}\\ \frac{1}{\rho_0}\tau_{\xi i,j}^{0}\end{pmatrix}, \tag{30}$$

in which $\tau_{\xi i,j}^{0}$, $\tau_{\xi i,j}^{h}$ are the shear stresses in the ξ-direction at the free surface (wind stress) and at the base (bottom friction). The second derivative with respect to σ can now be performed as before, yielding

$$\begin{aligned}\delta_\sigma\left(\frac{4\overline{\nu_V}^{\xi}}{\overline{h}^{\xi}\overline{m}^{\xi}\overline{n}^{\xi}}\delta_\sigma \boldsymbol{u}_{i,j}^{n+1}\right) &= \frac{2}{\overline{m}^{\xi}\overline{n}^{\xi}}\boldsymbol{C}_{DZ}\begin{pmatrix}\frac{1}{\rho_0}\tau_{\xi i,j}^{h}\\ \frac{2\overline{\nu_V}^{\xi}}{\overline{h}^{\xi}}\boldsymbol{C}_{DZ\beta}\boldsymbol{u}_{i,j}^{n+1}\\ \frac{1}{\rho_0}\tau_{\xi i,j}^{0}\end{pmatrix} \\ &= \frac{2}{\rho_0\overline{m}^{\xi}\overline{n}^{\xi}}\boldsymbol{C}_{DZa}\tau_{\xi i,j}^{h} + \frac{4}{\rho_0\overline{h}^{\xi}\overline{m}^{\xi}\overline{n}^{\xi}}\boldsymbol{C}_{DZb}(\overline{\nu_V}^{\xi}\boldsymbol{C}_{DZ\beta})\boldsymbol{u}_{i,j}^{n+1} \\ &\quad + \frac{2}{\rho_0\overline{m}^{\xi}\overline{n}^{\xi}}\boldsymbol{C}_{DZc}\tau_{\xi i,j}^{0}.\end{aligned} \tag{31}$$

Here, the expression $\overline{\nu_V}^{\xi}\boldsymbol{C}_{DZ\beta}$ denotes successively,

- the first line of $\boldsymbol{C}_{DZ\beta}$ times $\overline{\nu_{V_{i,j,1}}}^{\xi}$,
- the second line of $\boldsymbol{C}_{DZ\beta}$ times $\overline{\nu_{V_{i,j,2}}}^{\xi}$,

  $\vdots$
- the $((N-1)$-st) line of $\boldsymbol{C}_{DZ\beta}$ times $\overline{\nu_{V_{i,j,N-1}}}^{\xi}$,

since $\overline{\nu_V}^{\xi}$ is, in general, a function of σ. The second term on the right-hand side of (31) contains the unknown variable $\boldsymbol{u}_{i,j}^{n+1}$ at the new time level is now moved to the left-hand side of the equation; the first and the third term remain for all times on the right-hand side because they are prescribed through the boundary conditions. In this way the following

TABLE 1

Comparison of the Maximal Time-Step Sizes Necessary for Stable Integrations of Lake Constance Circulations when Explicit and Semi-Implicit (in the σ-Direction) Temporal Discretizations Are Used

	Homogeneous water		Stratified water	
N (number of polynomials)	6	12	6	12
Δt [s] explicit	7.2	1.5	7.2	1.5
Δt [s] σ-implicit	1440	1440	144	144

system of linear equations is obtained

$$\boldsymbol{A}^n_{i,j} \begin{pmatrix} \Phi^{n+1}_{i,j,0} \\ \Phi^{n+1}_{i,j,1} \\ \vdots \\ \Phi^{n+1}_{i,j,N} \end{pmatrix} = \boldsymbol{B}^n_{i,j}, \tag{32}$$

where $\boldsymbol{A}^n_{i,j}$ is a fully occupied $(N+1) \times (N+1)$ matrix and $\boldsymbol{B}^n_{i,j}$ is a $(N+1) \times 1$ matrix, known on the old time level n. With such a system, for each (i, j) the field variables u, v (of the momentum balance in the ξ- and η-directions) and temperature T can be separately determined by using (24), (25), and (26).

Test computations have shown that the largest time steps that are tolerated in order that the "σ-implicit" scheme can stably be integrated is larger than in the explicit method: (i) in wind induced computations of Lake Constance by a factor between 200 (for $N = 6$) and 800 (for $N = 12$) if the lake water is homogeneous and (ii) between 20 (for $N = 6$) and 80 (for $N = 12$) if it is stratified. The results depend somewhat on the number of Chebyshev polynomials that are used (see Table 1). However, the computational times can be reduced, respectively, approximately by a factor of 60 for homogeneous water and 6 for stratified water in comparison with the explicit scheme, since the computational time for a time step with the σ-implicit scheme is larger than that with the explicit scheme. This factor of computational time reduction is only slightly dependent on the number of Chebyshev polynomials that is used.

Results obtained with the explicit and semi-implicit schemes and compared showed an excellent agreement. This corroborated that the two discretizations are equivalent to each other.

4. STABILITY PERFORMANCE

In this section the stability of the proposed numerical schemes is studied for both the semi-implicit in the σ-direction and explicit time integration for Lake Constance, an Alpine lake bordening Germany, Austria, and Switzerland. It consists of three basins: Obersee, Überlinger See, and Untersee, but the Untersee is separated from the other two basins by the 5-km long channel "Seerhein"; we shall here be concerned with the ensemble Obersee+Überlinger See, for brevity also referred to as Lake Constance. It is approximately

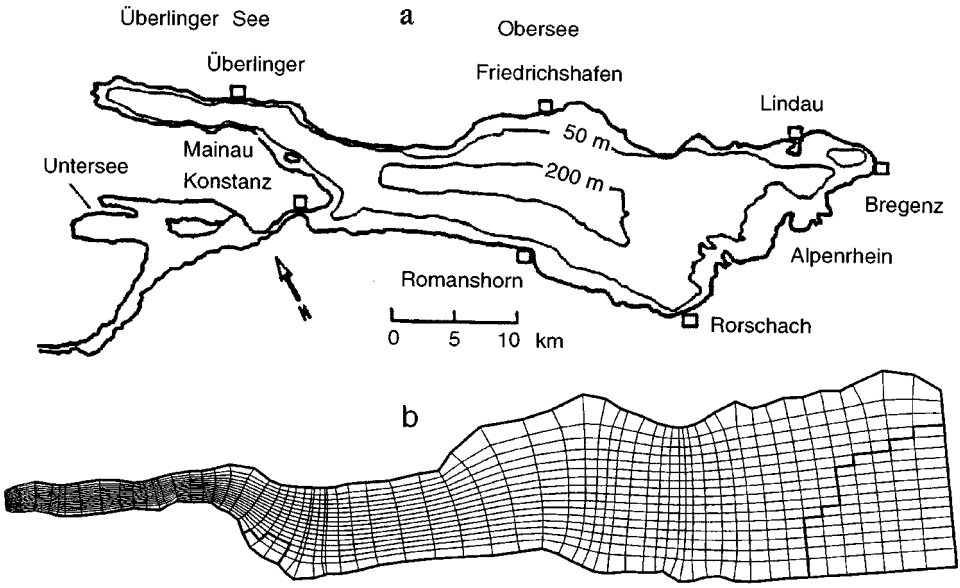

FIG. 1. (a) Map of Lake Constance. Untersee, Überlinger See, and Obersee. Also shown are the 50 m and 200 m isobaths and a few main towns along the shore. (b) Distribution of horizontal curvilinear coordinate net with computational shoreline (heavy solid line) with resolution $L \times M = 65 \times 17$.

64 km long and 16 km wide, has a maximum depth of 250 m and an approximate mean depth of 100 m (Fig. 1a). The Überlinger See is a relatively deep and narrow arm, "separated" from the main upper lake by a sill just west of the island Mainau. The depth discretization we use in this paper is based on the bathymetric map of the 1990 survey [43]. The smallest depth in the computations is assumed to be 10 m. The discretization is shown in Fig. 1b with grid points $L \times M = 65 \times 17$, while in the vertical direction six or more polynomials are used. A large number of test runs, in which the austausch terms, the time step, and the mesh size were varied, was performed to scrutinize the stability performance of the code.

4.1. *Homogeneous Water*

For simple wave-like problems with explicit schemes, instability, occurs in general, when the Courant–Friedrichs–Levy (CFL) criterion,

$$V_{\max} \leq \Delta s/(\sqrt{2}\Delta t), \tag{33}$$

is violated; here, Δs denotes the smallest mesh size, Δt is the time step, and $V_{\max}$ is the maximal phase speed of the wave. With $\Delta s = 500$ m, $\Delta t = 86.4$ s (1 day = 1000 time steps) this velocity is 4.1 m s^{-1}. It is much smaller than the barotropic shallow water speed; since the rigid-lid assumption eliminates surface gravity waves, the equations only incorporate the topographically induced barotropic motions whose velocities are small. The CFL condition therefore does not need to conform with the high speed barotropic Kelvin and Poincaré waves which would otherwise severely constrain the time step of the explicit scheme. When diffusion is included, the stability issue becomes more complicated. If, owing to small friction, large gradients in the field variables can build up or numerical

noise be formed, then the computations often lead to violations of the CFL condition and instabilities form. A balance of horizontal diffusive terms and inertial terms leads, through a dimensional argument to the *damping* (*viscous*) *time scale*

$$[T_H] = (\Delta x)^2/(\pi^2 \nu_H) \tag{34}$$

(the factor π^2 in the denominator is not important, other estimates replace it by 2) for the shortest waves that can be modelled by the equations. This time should be short enough to damp out the numerical noise and long enough on the larger scales to retain the features one is interested in. For instance with $\nu_H = 1.0\,\mathrm{m^2\,s^{-1}}$ and $\Delta x = 500$ m this yields $[T_H] \sim 1$ day. In other words, with horizontal diffusivities of $1.0\,\mathrm{m^2\,s^{-1}}$ periods of processes of less than approximately 1 day cannot be resolved. Should they be significant, then one must work with a smaller horizontal mesh size. An analogous argument works equally in the vertical direction with $[T_V] = (\Delta z)^2/(\pi^2 \nu_V)$.

To explore the stability range of the explicit code, computations were performed by using a constant uniform wind in the long direction with wind stress $\tau^0 = 0.05\ N\ \mathrm{m^{-2}}$ ($\sim 4.7\ \mathrm{ms^{-1}}$ windspeed), a resolution of $L \times M \times N = 65 \times 17 \times 6$ mesh points, a time step $\Delta t = 7.2$ s, horizontal diffusivity $\nu_H = 1.0\ \mathrm{m^2\,s^{-1}}$ and constant vertical diffusivities ν_V as shown in Table 2. It displays the number of time steps through which computations could proceed and at which the numerical break down occurred. Evidently, the duration of stable integration increases with increasing ν_V until stable computations are possible for $\nu_V \in [0.02, 0.05]\,\mathrm{m^2\,s^{-1}}$; for even larger values of ν_V the time step is then too large to resolve the vertical diffusion. For $\nu_V = 0.1\,\mathrm{m^2\,s^{-1}}$ the vertical diffusive time scale $[T] = \Delta z^2/(\pi^2 \nu_V)$ is approximately 4 s, if $\Delta z = 2$ m, a value approximately corresponding to the smallest vertical nodal point distance. Processes on this time scale, however, are no longer properly resolved by our time step $\Delta t = 7.2$ s. If, on the other hand, the time step is decreased to $\Delta t = 3$ s (28800 steps per day!) the code delivers physically acceptable results with $\nu_V = 0.1\,\mathrm{m^2\,s^{-1}}$.

Generally, the diffusivities should not and cannot be chosen independently of the choice of the time step. According to experience and owing to measured values (see [37, 40] for a summary, [51, 48]) values of $\nu_V = 0.1\,\mathrm{m^2\,s^{-1}}$ are too large; this is why we chose $\nu_V = 0.02\,\mathrm{m^2\,s^{-1}}$ for homogeneous water, which also satisfies the stability requirements. In [65] we shall go more deeply into this question and choose values of ν_V that vary with depth but remain of the order $0.02\,\mathrm{m^2\,s^{-1}}$.

What is the influence of the horizontal diffusivities ν_H? Table 3 collects the time steps of breakdown for the explicit code, when $\nu_H \in [0.05, 500]\,\mathrm{m^2\,s^{-1}}$ while $\nu_V = 0.02\,\mathrm{m^2\,s^{-1}}$ is

TABLE 2

Breakdown Times (Number of Time Steps) of Stable Computation for Lake Constance for Different Vertical Austausch Coefficients ν_V at Fixed $\nu_H = 1.0\ \mathrm{m^2\,s^{-1}}$ for the Explicit Code with a Time Step $\Delta t = 7.2$ s

ν_V : [$\mathrm{m^2\,s^{-1}}$]	0.005	0.01	0.02–0.05	0.07	0.1
Number of time steps for stable computations	19500	32000	Stable	40	30

TABLE 3

Breakdown Times (Number of Time Steps) of Stable Computation for Lake Constance for Different Horizontal Austausch Coefficients $\nu_H \in [0.05, 500]$ m^2 s^{-1} at Fixed $\nu_V = 0.02$ m^2 s^{-1} for the Explicit Code with a Time Step $\Delta t = 7.2$ s

ν_H: [m^2 s^{-1}]	0.05	0.1	0.5–200.0	300.0	500.0
Number of time steps for stable computations	19860	24030	Stable	70	30

kept constant, $\Delta t = 7.2$ s, and $\tau^0 = 0.05\ N\ \mathrm{m}^{-2}$. Evidently, for $\nu_H \in [0.5, 200]\ \mathrm{m}^2\ \mathrm{s}^{-1}$, the performance of the explicit code is stable. However, it should also be possible to perform stable computations with even larger horizontal friction coefficients; this is indeed the case, for instance, for $\nu_H = 500\ \mathrm{m}^2\ \mathrm{s}^{-1}$ if $\Delta t = 3$ s. Realistically, oceanographers and physical limnologists recommend $\nu_H = 1\ \mathrm{m}^2\ \mathrm{s}^{-1}$ (see [15]), but observations point also at smaller values [41].

These explicit code analyses thus indicate that numerical instabilities always arise if the diffusivities ν_H and/or ν_V are not sufficiently large to avoid or attenuate numerical noise. Numerical instabilities can also arise with (very) large values of the austausch coefficients, if the time steps are too large to resolve he (vertical) diffusion; however, if the time steps are sufficiently small, stability can always be reached with large diffusivities. Should the smallest values of the diffusivities ν_H, ν_V necessary to achieve stable integration be larger than physically tolerable, then the horizontal and/or vertical mesh sizes can be reduced and the number of Chebyshev polynomials increased to stabilize the computation at reduced values of the diffusivities. For instance, if one chooses $L \times M = 129 \times 33$ in the horizontal, $\nu_H = 0.1\ \mathrm{m}^2\ \mathrm{s}^{-1}$ and $\Delta t = 1.5$ s, one obtains stable performance of the code in our example.

Interesting in this context is also the fact that with variable mesh size (in the curvilinear orthogonal coordinate system) a variable horizontal austausch coefficient that is adjusted to the local grid size may lead to better results than a constant coefficient. The adjustment must be such that the austausch coefficient ν_H is the larger, the larger the local mesh size is.

Tables 2 and 3 also show that the explicit model for Lake Constance with 65×17 mesh points and six Chebyshev polynomials is computationally stable if the austausch coefficients are chosen as $\nu_H = 1.0\ \mathrm{m}^2\ \mathrm{s}^{-1}$, $\nu_V = 0.02\ \mathrm{m}^2\ \mathrm{s}^{-1}$, and $\Delta t = 7.2$ s; from a limnological point of view this time step is too small, yet a substantial increase is not possible because with $\Delta t = 10$ s the code performs unstably. It can also be, and has been, verified that stable numerical integration with $\Delta t = 7.2$ s is also possible, if ν_H is as large as $200\ \mathrm{m}^2\ \mathrm{s}^{-1}$, but not if ν_V is only slightly enlarged over its "stable" value $0.02\ \mathrm{m}^2\ \mathrm{s}^{-1}$ (since such a change would have to go along with a reduction of Δt). This means that the restriction of the time step for this explicit code primarily stems from the diffusion in the vertical direction; in other words, the time step is restricted by the larger vertical austausch coefficient and the smallest distance of the vertical nodal points.

As already mentioned in Section 2 the vertically integrated flow and the baroclinic circulation (whose vertically integrated flow vanishes) are solved separately. The advantage is that one does not need to explicitly compute the pressure gradient at the free surface which is unknown due to the rigid-lid assumption. Test runs have also shown that with the explicit

TABLE 4

Breakdown Times (Number of Time Steps) of Stable Computation for Lake Constance for Different Vertical Austausch Coefficients $\nu_V \in [0.005, 10000]$ m^2 s^{-1} at Fixed $\nu_H = 1.0$ m^2 s^{-1} for the "σ-Implicit" Code with a Time Step $\Delta t = 24$ min

ν_V: [m^2 s^{-1}]	0.005	0.01	0.02–2000.0	5000.0	10000.0
Number of time steps for stable computations	50	160	Stable	140	50

code much larger time steps can be used for the vertically integrated barotropic circulation processes than for the baroclinic one if one employs two different time steps for the two flow components. Likely reasons for the property are: first, the limitation of the time step in the explicit scheme comes from the vertical direction; however, the barotropic component to the currents does not depend on the vertical direction. Second, and despite the fact that an explicit temporal integration is used for both the barotropic and baroclinic components, the barotropic current must, in the entire domain, at the new time step be computed by a coupled procedure; i.e., it should also incorporate the fields that are unknown at the new time level, which improves the stability of the integration scheme. For this reason, the implicit scheme for the barotropic current component should be avoided, which is indeed the case in our code where the "σ-implicit" time integration is only employed for the baroclinic component of the total motion.

Tables 4 and 5 collect the number of time steps for the break down of the "σ-implicit" code when several different horizontal and vertical austausch coefficients are selected in the intervals $\nu_V \in [0.005, 10000]$ m^2 s^{-1} and $\nu_H \in [0.05, 5.0]$ m^2 s^{-1}, respectively; the time step was $\Delta t = 24$ min and is 200 times large than for the explicit scheme. The qualitative behaviour is very similar to the previous, explicit case. For very small, and again for very large, ν_V-values the "σ-implicit" scheme is not stable. While the numerical instabilities at very large values of $\nu_V \geq 5000$ m^2 s^{-1} are unphysical, those at $\nu_V \leq 0.01$ m^2 s^{-1} are more bothersome because these values are within the physically acceptable range. Unfortunately for variable ν_H, the range of ν_H-values of stable performance of the code is rather narrow ($\nu_H \in [0.5, 1.0]$ m^2 s^{-1} for $\nu_V = 0.02$ m^2 s^{-1}). Remedy requires increase of the horizontal spatial resolution and/or reduction of the time step. It implies also that the time-step size is only restricted by the horizontal direction, because implicit integration is already applied in the vertical direction. Incidentally, stable integration would also be possible with

TABLE 5

Breakdown Times (Number of Time Steps) of Stable Computation for Lake Constance for Different Horizontal Austausch Coefficients $\nu_H \in [0.05, 50]$ m^2 s^{-1} at Fixed $\nu_V = 0.02$ m^2 s^{-1} for the "σ-Implicit" Code with a Time Step $\Delta t = 24$ min

ν_H: [m^2 s^{-1}]	0.05	0.1	0.5–1.0	2.0	5.0
Number of time steps for stable computations	110	130	Stable	40	20

$\nu_H = 0.5\,\mathrm{m^2\ s^{-1}}$, $\nu_V = 0.02\,\mathrm{m^2\ s^{-1}}$, and a time step $\Delta t = 48$ min; however, in order to limit the discretization errors such a procedure is not recommended.

We summarize our findings as follows:

- At fixed spatial resolution the austausch terms ν_V and ν_H must be sufficiently large to guarantee that numerical oscillations (noise) are attenuated, and computations can stably be executed. Tables 2 and 3 list conditions for the explicit code, Tables 4 and 5 those for the implicit code.
- Time steps are restricted by the austausch terms and the spatial resolution; for the σ-implicit temporal integration this dependence is chiefly dictated by the horizontal diffusion coefficient and the horizontal spatial resolution. Computations that are not stable at very large values of the diffusivities at a given time step can be stabilized by a reduction of the time step (see Tables 2 and 3).
- For given ν_V, ν_H stable performance of the explicit or semi-implicit codes can, in principle, always be achieved by reducing the mesh size or increasing the number of model points. With $\nu_V = 0.005\,\mathrm{m^2\ s^{-1}}$ and $N = 18$ Chebyshev polynomials instead of $N = 6$ (see Tables 2 and 4) the explicit code performs stably provided the time step is also reduced from $\Delta t = 7.2$ s to $\Delta t = 0.5$ s (172,800 steps per days!), while the σ-implicit code computation is stable with the same time step $\Delta t = 24$ min as that with $N = 6$.

4.2. *Stratified Water*

The qualitative behaviour of the stability performance in stratified water is very similar to the previous, homogeneous case. However, in the stratified case some additional difficulties arise which are traceable to the temperature profile as a cause. Test computations for wind-induced currents have shown that the relatively coarse resolution in the vertical direction and the relatively small vertical diffusivities ν_V at the metalimnion depth are prone to numerical instabilities. The numerical oscillations (noise) have no physical bearing, are due to the FD-approximation and essentially inavoidable, but can be delimited by the mesh size and the number of Chebyshev polynomials in the spectral expansion. In the horizontal direction, the numerical diffusion and, thus, the spurious oscillations constitute no difficulties for the performance of the code, because the horizontal temperature gradients and current changes are generally small. In the transition layer from the epi- to the hypolimnion the vertical temperature gradients and the gradients of the baroclinic currents are, however, large; in addition, the physical, vertical diffusivities ν_V are small and, correspondingly, the spurious oscillations in the computed variables, large. For reasons of numerical stability ν_V should, in the metalimnion, be large at the relatively coarse mesh size we chose, certainly larger than is physically justified. With a refined vertical resolution a reduction of the artificial numerical diffusion, which is overshadowed by the physical diffusion, should be achieveable. Such a goal can only be reached by increasing the necessary CPU-times.

In SPEM the nodal points σ_n are positioned at the extrema of the Chebyshev polynomials of order N. Thus, the vertical nodal-point distances are not uniform, but smaller close to the bottom and close to the free surface, with fairly coarse resolution in the middle, whence also in the metalimnion. For instance, for a 100-m deep lake with $N = 12$ the nodal point distances are the largest between 15 m and 50 m depth, where the metalimnion is situated. This explains, at least heuristically, why the code did not achieve numerical stability when

the austausch coefficients assumed the relatively large values

$$\begin{aligned} \nu_H &= 1.0\ \mathrm{m^2\,s^{-1}}, \quad \nu_V = 0.02\ \mathrm{m^2\,s^{-1}}, \\ D_H^T &= 1.0\ \mathrm{m^2\,s^{-1}}, \quad D_V^T = 0.0005\ \mathrm{m^2\,s^{-1}}, \end{aligned} \tag{35}$$

and the initial temperature profile in °C was given by

$$T(t=0) = \begin{cases} 17 - 2\exp(-(z+10)/5), & z \geq -20\ \mathrm{m}, \\ 5 + 10\exp((z+10)/20), & z < -20\ \mathrm{m}, \end{cases} \tag{36}$$

which is realistic for summer stratification and whose maximal vertical gradient arises between 10 and 30 m. Evidently, between the epi- and hypolimnion the vertical diffusivities should, for numerical stability be larger, which, however, would physically not be meaningful. Test runs have also shown that numerical stability can be reached with the vertical diffusivities (35), if the initial vertical temperature profile is changed such that the largest vertical gradient does no longer arise between 10 m and 30 m but at the free surface. This is the case, e.g., for the initial temperature profile

$$T(t=0) = 5 + 15\exp(z/20) \quad [^\circ\mathrm{C}]. \tag{37}$$

Better stability conditions should also be obtainable if the number of polynomials is enlarged. Indeed, if one chooses $N = 18$, instead of $N = 12$, the run with the initial temperature profile (36) and the diffusivities (35) remains stable; all the more, the diffusivities (35) can even be slightly reduced and better adjusted to values closer to physical reality. Physically meaningful, nonconstant vertical distributions of the horizontal and vertical diffusivities are

$$\begin{aligned} \nu_V &= \begin{cases} 0.04, & z > -20\ \mathrm{m}, \\ 0.01, & -20\ \mathrm{m} \geq z \geq -40\ \mathrm{m}, \\ 0.02, & z < -40\ \mathrm{m}, \end{cases} \quad [\mathrm{m^2\,s^{-1}}], \\ \nu_H &= 1.0\ \mathrm{m^2\,s^{-1}} \quad \text{(constant)}, \\ D_V^T &= \begin{cases} 0.0005, & z > -20\ \mathrm{m}, \\ 0.0001, & -20\ \mathrm{m} \geq z \geq -40\ \mathrm{m}, \\ 0.0002, & z < -40\ \mathrm{m}, \end{cases} \quad [\mathrm{m^2\,s^{-1}}], \\ D_H^T &= 1.0\ \mathrm{m^2\,s^{-1}} \quad \text{(constant)}, \end{aligned} \tag{38}$$

and for these, computations with 18 Chebyshev polynomials are stable.

5. CONVERGENCE PROPERTIES

So far the convergence properties of the model were not discussed. Because of the spectral expansion in the vertical we expect these to be better than if finite differences or layers would have been used.

By decreasing the mesh size and increasing the number of Chebyshev polynomials increasingly improved approximations of the velocity and temperature fields can be obtained. Our standard choice $L \times M = 65 \times 17$ corresponds in Lake Constance approximately to a

mean grid length of $\Delta x \simeq \Delta y \simeq 1$ km, not uniformly distributed over the lake. Uniformity in grid size distribution is intended, because the numerical oscillations preferably occur on the small scales; however, it is difficult to achieve. In a rectangular basin this problem is irrelevant as no Schwarz–Chrystoffel transformation must be performed.

In principle, each attempt to estimate the discretization error is based on a comparison of results obtained with different mesh sizes (leaving all other things equal). To test this, computations of wind-induced motions in a rectangle of 65×17 km^2 extent and 100 and 200 m constant depth, respectively, were performed for homogeneous water and a uniform wind of 4.7 ms^{-1} speed, constant in time. The horizontal mesh size was chosen to be 1 km, and computations were performed for different vertical resolutions, using 6, 12, and 18 Chebyshev polynomials, respectively, and different vertical diffusion coefficients, $\nu_V = 0.02$ m^2 s^{-1} and $\nu_V = 0.005$ m^2 s^{-1}, keeping the horizontal diffusivity fixed at $\nu_H = 1.0$ m^2 s^{-1}. Furthermore, variations of the horizontal mesh size showed this to have negligible effects on the solution except in the vicinity of shores and when tracer diffusion is considered. We display the vertical profiles of the three velocity components at the mid-lake position four days after the onset of the wind—corresponding nearly to steady state conditions. In addition, we compare time series of the total kinetic energy stored in the water. Figure 2 shows the computed vertical distributions of the velocity components u (x-direction, with the wind), v (y-direction), and w (vertical direction, vanishingly small in comparison to the u- and v-components). Figure 3 shows the corresponding time series of the total kinetic energy. The water depth was 100 m. The curves do not differ much from one another; only very small differences in the u- and v-profiles and the time series of the total kinetic energy can be discerned between those computed with six and 12 polynomials. Increasing the mode number to even more polynomials (e.g., $N = 18$), would

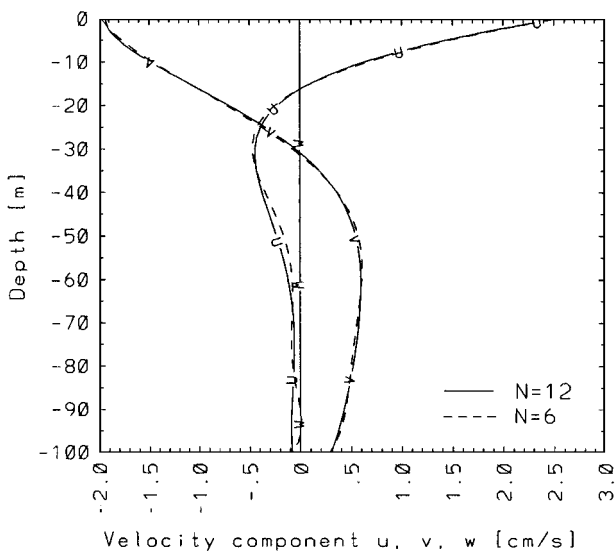

FIG. 2. Vertical profile of the three velocity components u, v, and w in the midpoint of the homogeneous rectangular basin of constant depth ($h = 100$ m) for 4 days after constant west wind setup, with the vertical diffusivities $\nu_V = 0.02$ m^2 s^{-1}. The broken curves were obtained with $N = 6$ Chebyshev polynomials, the solid curves with $N = 12$.

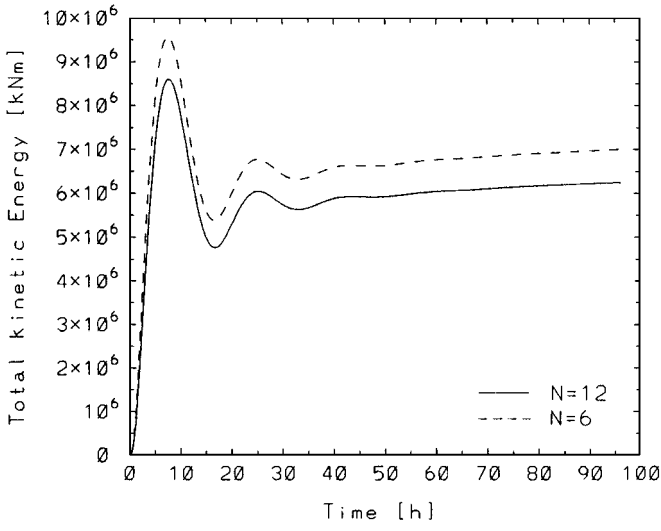

FIG. 3. Time series of the kinetic energy in the homogeneous rectangular basin of constant depth ($h = 100$ m) subject to constant west wind with the vertical diffusivities $\nu_V = 0.02$ m^2 s^{-1}. The broken curves were obtained with $N = 6$ Chebyshev polynomials, the solid curves with $N = 12$.

not increase the accuracy of the results beyond that in Figs. 2 and 3. On the other hand, when $\nu_V = 0.005$ m^2 s^{-1} and $h = 100$ m, computations with six polynomials are unstable; with 12 they are stable. However convergence is only reached with 18 Chebyshev polynomials as shown in Figs. 4 and 5. The substantially enhanced oscillatory nature of the circulation (with the inertial frequency) for the smaller values of the vertical diffusivities can be seen,

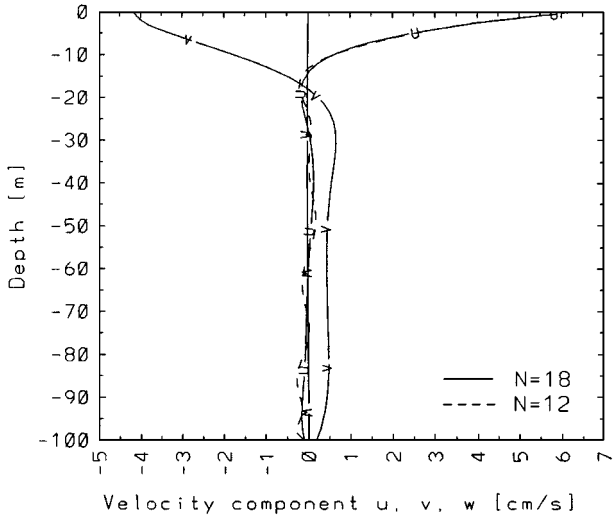

FIG. 4. Vertical profile of the three velocity components u, v, and w in the midpoint of the homogeneous rectangular basin of constant depth ($h = 100$ m) for 4 days after constant west wind setup, with the vertical diffusivities $\nu_V = 0.005$ m^2 s^{-1}. The broken curves were obtained with $N = 12$ Chebyshev polynomials, the solid curves with $N = 18$.

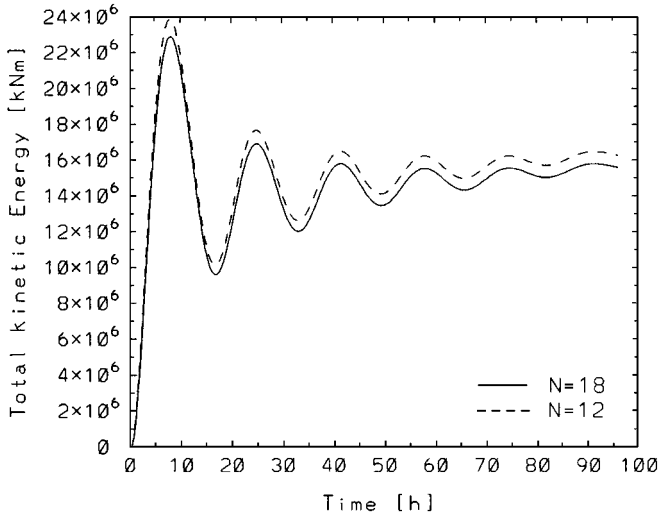

FIG. 5. Time series of the kinetic energy in the homogeneous rectangular basin of constant depth ($h = 100$ m) subject to constant west wind, with the vertical diffusivities $\nu_V = 0.005$ m^2 s^{-1}. The broken curve was obtained with $N = 12$ Chebyshev polynomials, the solid curve with $N = 18$.

if the kinetic energies of Figs. 3 and 5 are compared. Apart from this, the kinetic energy stored in the water for $\nu_V = 0.005$ m^2 s^{-1} is more than twice that for $\nu_V = 0.02$ m^2 s^{-1}. Qualitatively this is obvious, but quantitatively, it is nevertheless surprising.

Figures 6 and 7 display the anologous results for a 200 m deep basin. For ν_V 0.02 m^2 s^{-1}, results obtained with six polynomials are stable, but have not yet converged, while those

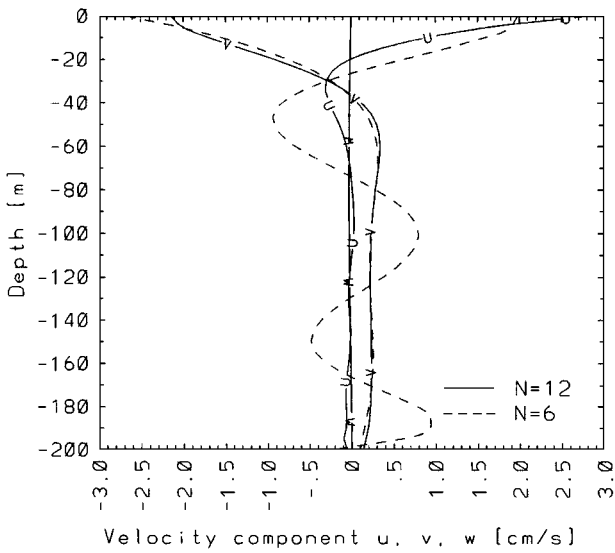

FIG. 6. Vertical profile of the three velocity components u, v, and w in the midpoint of the homogeneous rectangular basin of constant depth ($h = 200$ m) for 4 days after constant west wind setup, with the vertical diffusivities $\nu_V = 0.02$ m^2 s^{-1}. The broken curves were obtained with $N = 6$ Chebyshev polynomials, the solid curves with $N = 12$.

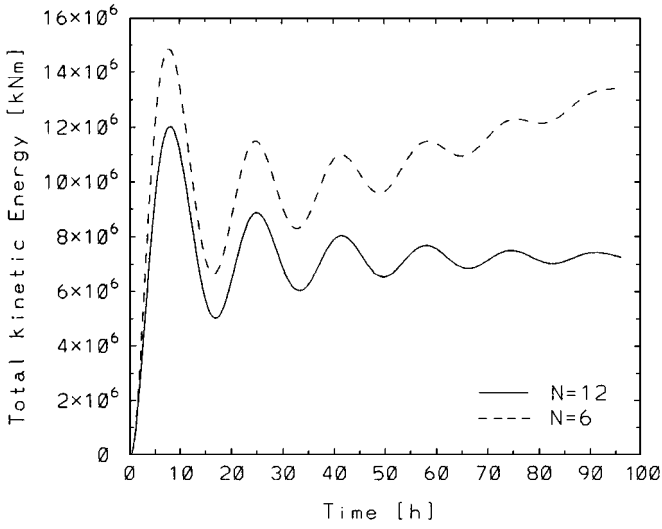

FIG. 7. Time series of the kinetic energy in the homogeneous rectangular basin of constant depth ($h = 200$ m) subject to constant west wind, with the vertical diffusivities $\nu_V = 0.02\ \mathrm{m^2\,s^{-1}}$. The broken curve was obtained with $N = 6$ Chebyshev polynomials, the solid curve with $N = 12$.

obtained with 12 polynomials have converged. Interestingly, (i) steady state is reached faster for the more accurate resolution and (ii) the oscillatory component in the motion is more pronounced for the case with 200 m depth than 100 m depth (compare Figs. 3 and 7).

In summary: the deeper a lake is and/or the smaller the vertical austausch coefficients of momentum are, the better must be the vertical resolution (i.e., the larger the number of considered Chebyshev polynomials) to obtain sufficiently accurate results. This behaviour is qualitatively the same as that deduced from stability considerations. Lake Constance has a maximum depth of 250 m and a mean depth of 100 m. This thus requires, to achieve reliable results, 12 polynomials when $\nu_V = 0.02\ \mathrm{m^2\,s^{-1}}$ and 18 or even more polynomials when $\nu_V = 0.005\ \mathrm{m^2\,s^{-1}}$.

6. EXAMPLES—TEST UNDER REALISTIC CONDITIONS

In this section we illustrate the model performance by demonstrating results obtained for circulation scenarios in an assumed rectangular basin with constant depth and in Lake Constance for both homogeneous and stratified water, respectively.

6.1. *Homogeneous Water*

Homogeneous Rectangular Basin with Constant Depth

Consider a rectangular basin of $65 \times 17\ \mathrm{km^2}$ extent and 100 m depth; assume homogeneous water, initially at rest, and subject to external wind-forcing. Let this wind blow in the long direction of the rectangle (from left, i.e., west), uniform in space, Heaviside in time, and with strength $0.05\,N\ \mathrm{m^{-2}}$ ($\simeq 4.7\ \mathrm{ms^{-1}}$ windspeed). This is the wind-forcing we apply throughout the paper. Integration starts at rest until steady state is reached. Let the discretization be implemented with $\Delta x = \Delta y = 1$ km. In computations $\nu_H = 1\ \mathrm{m^2\,s^{-1}}$ is kept constant, because it turned out that the numerical values of ν_H are not very crucial,

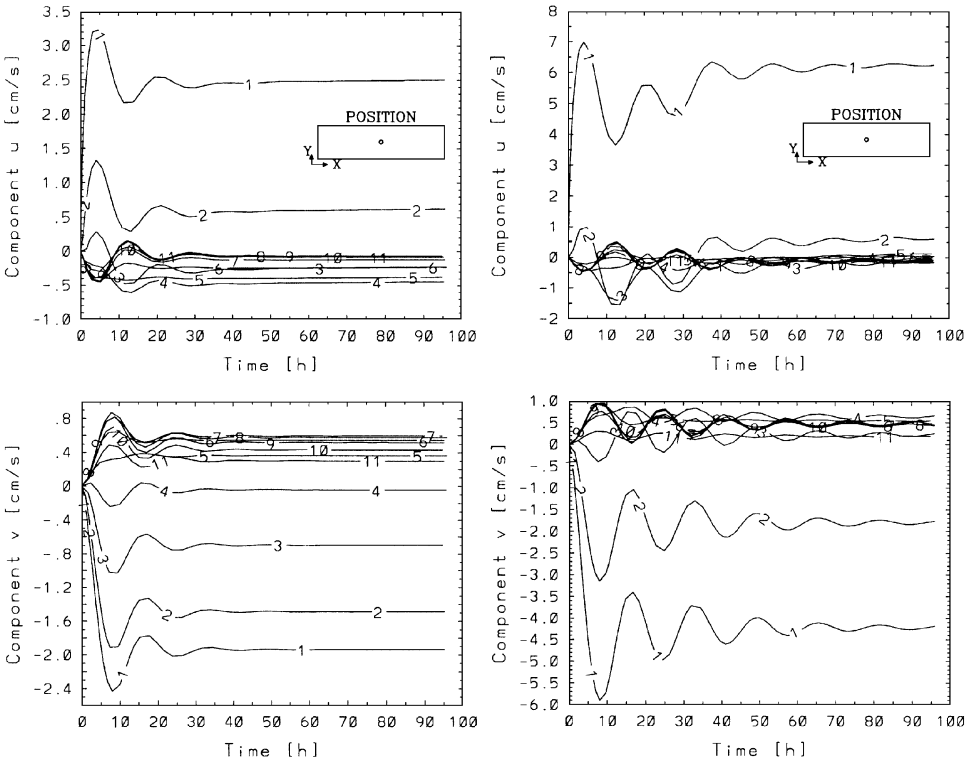

FIG. 8. Temporal evolution of the horizontal velocity components u (top) and v (bottom) for a midlake position in the homogeneous rectangular lake of constant depth subject to a Heaviside wind setup in the long direction. The symbols (1, 2, 3, ..., 11) refer to the depth (0, 10, 20, ..., 100) m. The graphs on the left are produced with $\nu_V = 0.02$ m^2 s^{-1}, those on the right for $\nu_V = 0.005$ m^2 s^{-1}.

while ν_V is, respectively, $\nu_V = 0.02$ m^2 s^{-1} (physically a large value) and $\nu_V = 0.005$ m^2 s^{-1} (physically a more realistic value). With the smaller value, $\nu_V = 0.005$ m^2 s^{-1}, stable computations must be performed with $N = 18$ polynomials instead of $N = 12$. That the values of vertical diffusivities are significant can be seen, when the transient response from initiation of the motion to steady state is analysed. We focus attention to time series of the horizontal velocities, u, v at 10 m depth intervals in the mid-lake position. Figure 8 (left) displays these for $\nu_V = 0.02$ m^2 s^{-1} (the larger value). Steady state conditions are approximately reached after less than 40 to 50 h, but initially an oscillating motion is superposed on the monotonic trend into steady state, which is identified with the inertial wave of 16.3-h period for $f = 1.07 \times 10^{-4}$ s^{-1}. This oscillating signal is damped away after less than two periods. The flow shows surface boundary layer structure, obviously reminiscent of the Ekman type with a thickness of approximately 40 m. By contrast in Fig. 8 (right), which shows the corresponding results for $\nu_V = 0.005$ m^2 s^{-1}, the inertial motions persist much longer. Furthermore, it is evident that the Ekman layer is thinner and more pronounced as the surface velocities are larger in Fig. 8 (right) than in Fig. 8 (left), and the decay with depth is faster.

In Fig. 9, the time series of the total kinetic energy in the homogeneous rectanglar basin of constant depth subject to constant west wind are displayed as before with the vertical diffusivities as indicated. As has been seen in the time series of the horizontal velocity, the

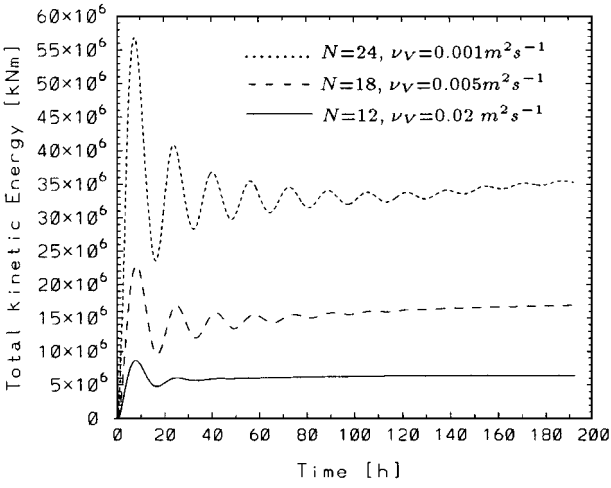

FIG. 9. Time series of the kinetic energy in the homogeneous rectangular basin of constant depth subject to constant wind from W.

inertial motions of the transient energy persist much longer with $\nu_V = 0.005\ \mathrm{m^2\,s^{-1}}$ than $\nu_V = 0.02\ \mathrm{m^2\,s^{-1}}$, and this is even more distinct for $\nu_V = 0.001\ \mathrm{m^2\,s^{-1}}$ and $N = 24$. It can also be seen that the total kinetic energy stored in the basin for $\nu_V = 0.001\ \mathrm{m^2\,s^{-1}}$ is much larger than for $\nu_V = 0.005\ \mathrm{m^2\,s^{-1}}$ or $\nu_V = 0.02\ \mathrm{m^2\,s^{-1}}$, which is due to the much larger energy input from wind stress because of the much larger water velocity at the free surface and the smaller dissipation for the smaller vertical diffusivity.

Table 6 summarizes the performance of the code when ν_V is varied; it lists the approximate number of oscillations seen in these inertial oscillations and gives rough estimates for the Ekman layer thickness and the asymptotic total kinetic energy. These results speak for themselves and point at the physical significance of the values of the vertical momentum diffusivities in homogeneous waters of enclosed lakes.

Homogeneous Lake Constance

An analogous study was also performed for Lake Constance with the same number of grid points (65×17) (see Fig. 1b) as for the rectangle. Computations were done also for

TABLE 6

For Three Values of the Vertical Austausch Coefficient ν_V and the Corresponding Values of the Number of Chebyshev Polynomials *N*, This Table Lists the Approximate Numbers of Inertical Oscillations, the Ekman Layer Thicknesses and the Values of the Total Kinetic Energy as Seen in Figure Like Figs. 8 and 9

ν_V [$\mathrm{m^2\,s^{-1}}$]	Number of Chebyshev polynomials	Number of oscillations seen	Ekman layer thickness [m]	Total kinetic energy $\times 10^6$ [kNm]
0.02	12	1–2	40–50	6.5
0.005	18	4–5	20–30	16.0
0.001	24	7–8	10–20	35.0

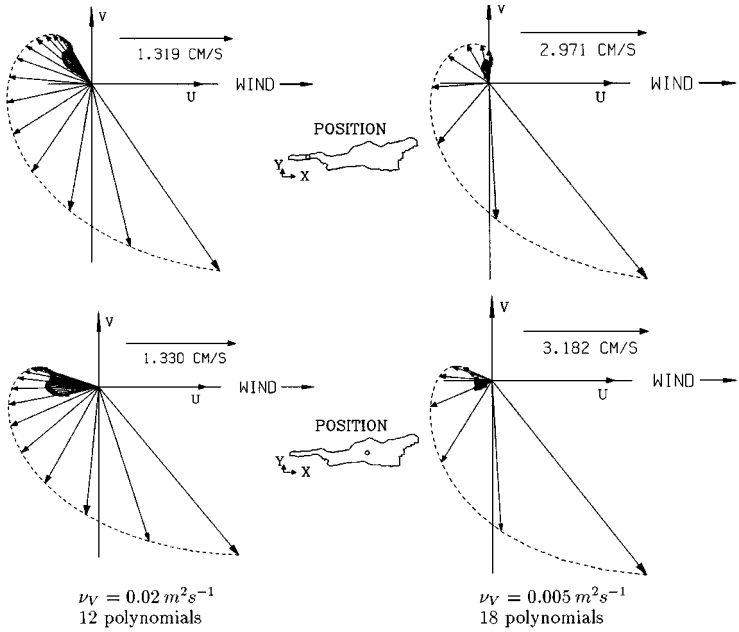

FIG. 10. Ekman spirals for a wind in the long direction of Lake Constance at the positions shown in the insets. The graphs show the horizontal velocities in two vertical profiles computed for large (left) and small (right) vertical diffusivities as indicated. The arrows are drawn for positions 5 m apart from one another from the free surface to the bottom.

$\nu_H = 1.0\ \mathrm{m^2\,s^{-1}}$ and $\nu_V = 0.02\ \mathrm{m^2\,s^{-1}}$ and $\nu_V = 0.005\ \mathrm{m^2\,s^{-1}}$, respectively. In the second case the larger number of polynomials $N = 18$ instead of $N = 12$ was needed to achieve stable numerical integration.

We display in Fig. 10 two steady Ekman spirals in the midlake positions of Überlinger See (left) and Obersee (right) as they form for an impulsively applied uniform wind from 305° (NW) (approximately in the long direction) and as obtained with the two different diffusivities. Those Ekman spirals are considerably affected by the ν_V values. The turning of the arrows making up the spirals also indicates that the surface Ekman boundary layer is thinner for the smaller values of the diffusivities (right panels) than for the larger ones (left panels). All this is qualitatively as one would physically expect.

Equally interesting is the comparison of the time series of the horizontal velocity components u and v for various depths in the midlake positions of Überlinger See and Obersee as displayed in Fig. 11, obtained with $\nu_V = 0.02\ \mathrm{m^2\,s^{-1}}$. At both positions transient oscillations can be discerned with the inertial period of ~16.3 h; steady state is reached after 4 days. The oscillations can be seen at all water depths, however with decreasing amplitude as the depth increases. Furthermore, they die out before 2 days in Überlinger See, but only after 4 days in the Obersee. Reason is the smaller size of Überlinger See and therefore the enhanced frictional resistance at the lake bottom and the side shores. Figure 11 also shows that the boundary layer close to the free surface is thick in the transverse velocity component and thin in the along-shore velocity component.

The time series of the stored, total kinetic energy in Lake Constance for $\nu_V = 0.02\ \mathrm{m^2\,s^{-1}}$ and $\nu_V = 0.005\ \mathrm{m^2\,s^{-1}}$ (Fig. 12) show that the inertial oscillations persist longer, and the

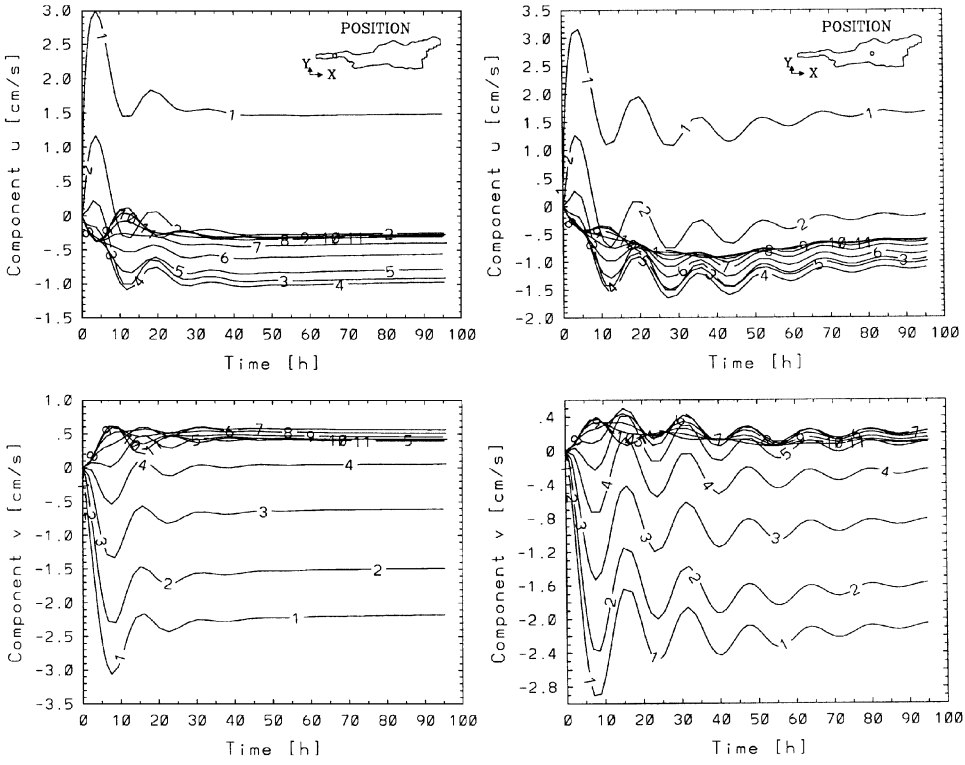

FIG. 11. Time series of the horizontal velocity components u (left) and v (right) in the midlake positions of Überlinger See (up) and Obersee (down) at various depths for impulsively started constant wind from 305° (NW) in the long direction of the lake. The labels (1, 2, 3, . . . , 11) correspond to the water depths (0, 10, 20, . . . , 100) m. Note that the number of oscillations that is visible is largely different in the two positions. $\nu_V = 0.02$ m^2 s^{-1}.

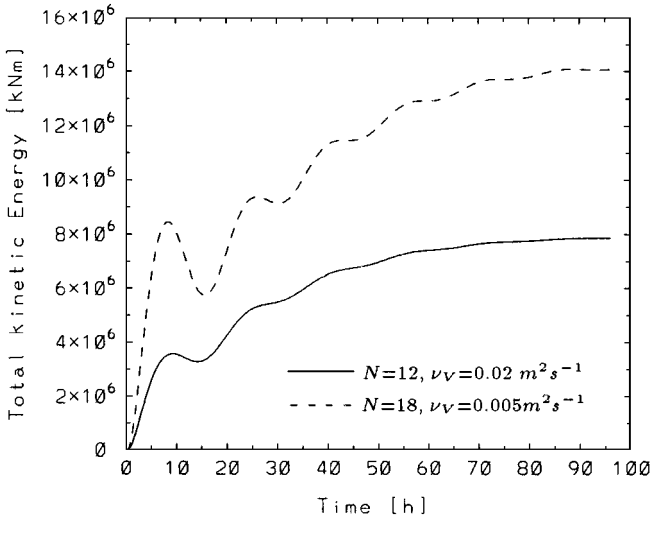

FIG. 12. Time series of the kinetic energy in the homogeneous Lake Constance subject to constant wind from 305° (NW). Result in the solid curve was obtained for $\nu_V = 0.02$ m^2 s^{-1}, that in the broken curve for $\nu_V = 0.005$ m^2 s^{-1}.

value of the total kinetic energy is much larger for the smaller ν_V-value, as shown before for the rectangular basin.

6.2. *Stratified Water*

The role played by the vertical diffusivities is even more crucial for the prediction of circulations in stratified water than it is for homogeneous water.

Stratified Rectangular Basin with Constant Depth

Computations were performed for the following diffusivities of momentum and heat:

- *Case* (i),

$$\begin{aligned} \nu_H &= 1.0\ \mathrm{m^2\,s^{-1}}, \quad D_H^T = 1.0\ \mathrm{m^2\,s^{-1}}, \\ \nu_V &= 0.02\ \mathrm{m^2\,s^{-1}}, \quad D_V^T = 0.0005\ \mathrm{m^2\,s^{-1}}, \end{aligned} \tag{39}$$

- *Case* (ii).

$$\begin{aligned} \nu_V &= \begin{cases} 0.04, & z > -20\ \mathrm{m}, \\ 0.004, & -20\ \mathrm{m} \geq z \geq -40\ \mathrm{m}, \\ 0.02, & z < -40\ \mathrm{m}, \end{cases} \quad [\mathrm{m^2\,s^{-1}}], \\ \nu_H &= 1.0\,\mathrm{m^2\,s^{-1}} \quad \text{(constant)}, \\ D_V^T &= \begin{cases} 0.0005, & z > -20\ \mathrm{m}, \\ 0.00005, & -20\ \mathrm{m} \geq z \geq -40\ \mathrm{m}, \\ 0.0001, & z < -40\ \mathrm{m}, \end{cases} \quad [\mathrm{m^2\,s^{-1}}], \\ D_H^T &= 1.0\,\mathrm{m^2\,s^{-1}} \quad \text{(constant)}, \end{aligned} \tag{40}$$

Case (i) assumes constant diffusivities with values unrealistically high; however, they were needed for numerical stability when (only) 12 Chebyshev polynomials were used. Case (ii) is more realistic as it accounts for smaller diffusivities (viscosities) in the metalimnion than in the epi- and hypolimnion. Compared with physically realistic values they are still somewhat large. As before, computations were performed for impulsively applied constant wind in the long direction from a state of rest during the first two days and an abrupt cessation afterwards; the lake is stratified by the initial vertical temperature [°C] profile

$$T(t=0) = \begin{cases} 17 - 2\exp(-(z+20)/5), & z \geq -20\ \mathrm{m}, \\ 5 + 10\exp((z+20)/20), & z < -20\ \mathrm{m}, \end{cases} \tag{41}$$

which is shown as curve A in Fig. 13. At the lake bottom and free surface vanishing heat flow is assumed.

Figure 13 shows two snapshots each of the midlake temperature profile 4 days (curves *B*) and 8 days (curves *C*), respectively, after the wind setup. The situation after 8 days corresponds to near steady conditions. Results in the broken curves were obtained with diffusivities (39), those in the solid curves with diffusivities (40). In the former the epilimnion temperature is lowered after 4 days by 2°C and again by 1.5°C during the subsequent 4 days. On the other hand, the hypolimnion temperatures rose by a few tenths of a degree.

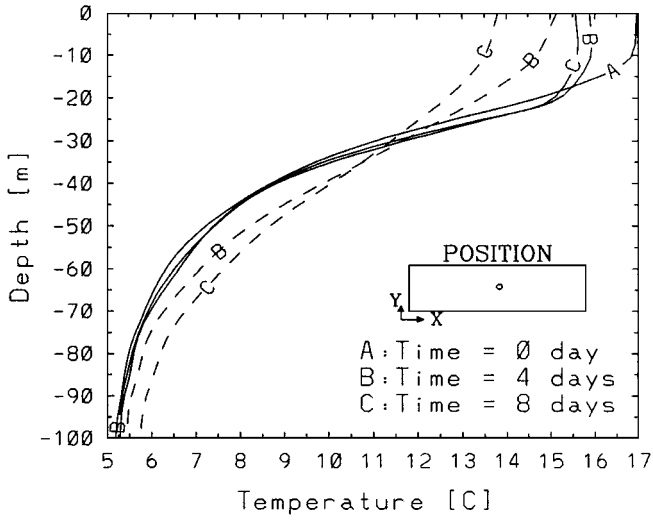

FIG. 13. Vertical distribution of the temperature in the midpoint of a rectangular basin, as given by formula (41) and initially (curves A) as well as 4 days (curves B) and 8 days (curves C) after a constant uniform wind with duration of two days had blown from the West, the solid curves as computed with the viscosities (40), the broken curves as obtained with the viscosities (39).

Turbulent mixing paired with diffusion is responsible for this behavior. The difference to the results displayed in solid curves shows how effective a reduction of the numerical values of the vertical diffusivities is. Now the maximum temperature drop in the epilimnion in 8 days is no more than 1.3°C, and the temperatures in the meta- and hypolimnion are hardly affected. The reason is the selection of the very small diffusivities in the metalimnion which block the erosion of the thermocline at larger depths, as physically required.

As was the case for the processes in homogeneous lakes, the smaller vertical diffusivities in (40) than in (39) let transient Kelvin- and Poincaré-type waves be developed while they are largely damped away before they are fully developed when the diffusivities (39) are selected. Figure 14 compares time series of the vertical velocity component w at 30 m depth at the four nearshore midpoints as obtained with the two sets of viscosities. Only from the solid curve results we can clearly identify two conspicuous components of oscillation. The longer periodic oscillation can be identified as an internal Kelvin-type wave the shorter one as a Poincaré-type wave, (see [66]).

Computations were also performed using 30 Chebyshev polynomials and reducing the viscosities even further. Because of numerical stability, the vertical diffusivities listed in (40) can only be reduced by approximately a factor of 0.6. Results are improved as compared to Figs. 13 and 14; in particular, the Kelvin wave shows up more conspicuously and is less quickly attenuated.

Stratified Lake Constance

It turned out that with the selection of diffusivities (40) and the initial temperature profile (41) no stable computations for the stratified Lake Constance could be achieved, unless more polynomials were used, which we eventually have not done. As already mentioned in the last section better conditions of numerical stability can be obtained if the region with

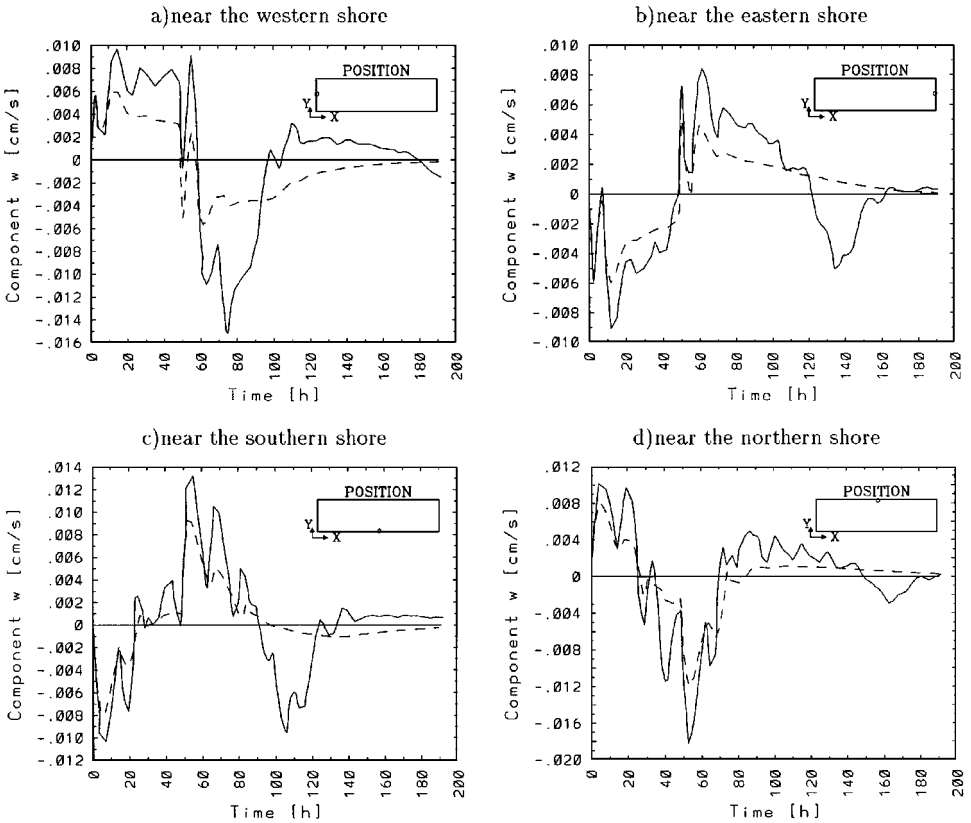

FIG. 14. Time series of the vertical velocity component w at the four indicated near-shore midpoints at 30 m depth in the inhomogeneous rectangular basin of constant depth subject to constant wind from West lasting two days. Results in solid curves were obtained with the nonconstant diffusivities (40), those in broken curves with the constant diffusivities (39).

large temperature gradients is better resolved; this means that the number of Chebyshev polynomials is increased or the metalimnion is closer to the free surface. The choice of 18 polynomials, the selection of the diffusivities according to (38) and the initial temperature profile (36) (whose largest temperature gradient is at 10 m depth instead of 20 m as in (41)) led to the stable computations.

Figure 15 shows time series of the vertical velocity component at the four indicated near-shore positions at various depths; these are computed for impulsively applied constant wind in the long direction (from 305°NW) with duration of two days. One can identify two components of oscillation; the longer periodic oscillation can be identified as an internal Kelvin type, the shorter as a Poincaré-type wave.

It is known that for wind-forcing in the transverse direction the Poincaré-type waves are more dominant. We also performed the computations under two-days transverse wind (from 215°SW). In Fig. 16 the time series of the horizontal velocity components u (top) and v (bottom) in the midlake positions of Überlinger See (left) and Obersee (right) at various depths are displayed. The Poincaré-type oscillations with the period of 4 h in Überlinger See (from v-component) and with the period of approximately 12 h in Obersee can clearly be identified, or which both were observed by Hollan [33].

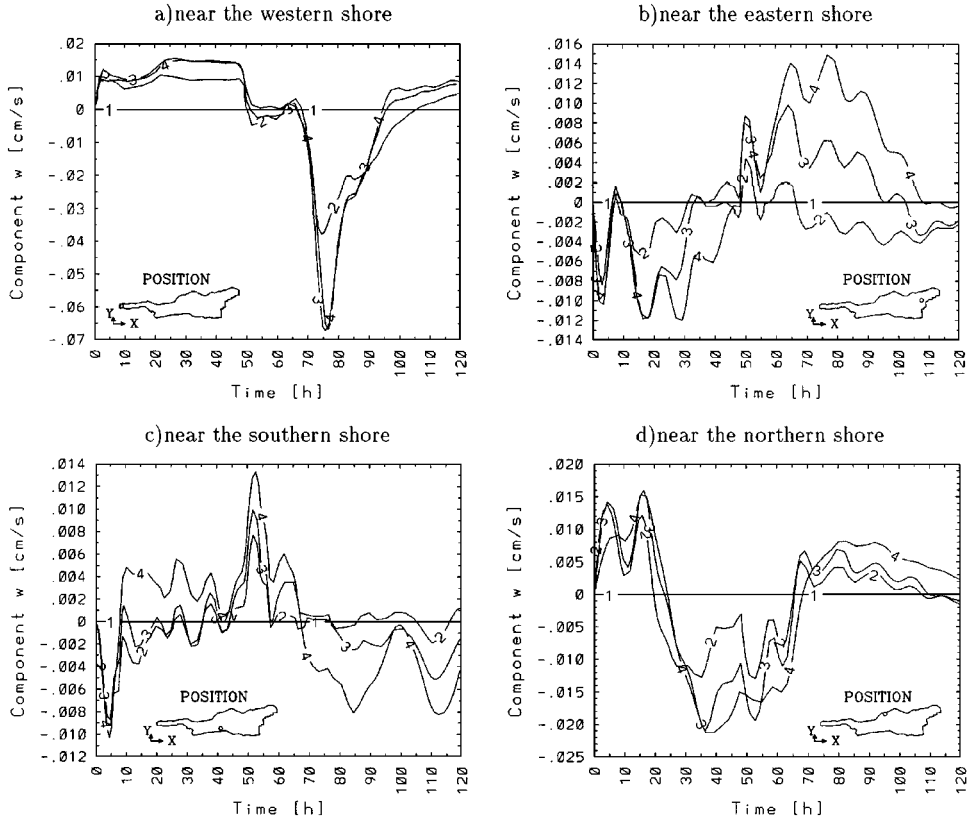

FIG. 15. Time series of the vertical velocity component w at the four indicated near-shore positions at various depths in the stratified Lake Constance subject to two days constant wind from 305° (NW). The labels (1, 2, 3, 4) correspond to the depths (0, 20, 40, 60) m. Results were obtained with the diffusivities (38) and initial temperature distribution (36).

7. CONCLUDING REMARKS

The barotropic and baroclinic circulation dynamics in inland lakes is driven by the meteorological input. The variation of the thermal structure is primarily established by the solar radiation and constitutes the long-term seasonal response for the lake. Once a certain thermal structure is established, it generally is maintained for a longer time (i.e., days or weeks); the currents, as responses to the external winds, are formed as time-dependent flows at a given stratification, which, under most situations, are weak insofar as they do not destroy this stable ground state, but introduce relatively small perturbations in the temperature field. During winter (i.e., from November to March at mid-latitude positions in the northern hemisphere) when the water is homogeneous, the temperature plays no role and barotropic currents are established. During summer a representative mean stratification can be assigned to a period of a few weeks. Under these conditions the barotropic currents are complemented by the much stronger baroclinic motions in which the mass distribution within the water body is of significance.

There are a large number of numerical models based on the shallow water equations in the Boussinesq approximation (e.g. [36, 46, 47, 50, 52, 53, 55, 57, 59–61, 63]). Haidvogel

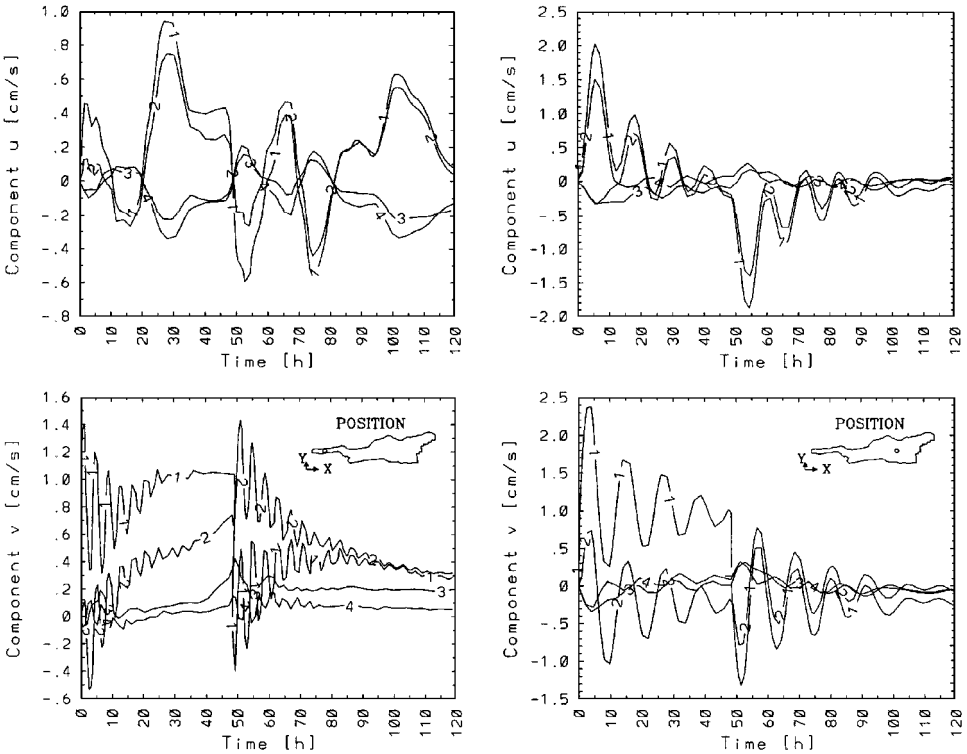

FIG. 16. Time series of the horizontal velocity components u (top) and v (bottom) in the midlake positions of Überlinger See (left) and Obersee (right) at various depths for impulsively started two days constant wind from 215° (SW) in the transverse direction of the lake. The labels (1, 2, 3, 4) correspond to the water depths (0, 20, 40, 60) m.

and Beckmann [8] summarized such models: DIECAST [18], DJM [17], GBM [19], GFDLM [14], GHERM [5], HAMSOM [3], ISPRAMIX [20], M3D [62], MICOM [10], POM [11], QUODDY [44], SCRUM [58], SEOM [45]); all claim to describe these kind of wind induced motions and have been applied to large scale oceanographic situations; some were employed to circulation flows in lakes and have had limited success (e.g., [9, 34, 36, 50, 55, 61]). However, these three-dimensional models or codes are limited in their applicability, or unsatisfactory, because internal wave processes are overly damped owing to the large explicit or implicit numerical diffusion that had to be built into the codes to stabilize them under common conditions. In this paper a three-dimensional nonlinear semispectral primitive equation model (SPEM) was presented having a semi-implicit temporal integration routine. It was applied to simple rectangular geometries as well as to Lake Constance with their water bodies being either homogeneous or stratified.

Because of the relatively small water depth, the smaller horizontal extent of lake basins and whence the significance of the boundaries in contrast to the ocean the explicit temporal integration in SPEM had to be replaced by a more stable semi-implicit integration routine. This made larger time steps of the integration routines possible and allowed, with defendable computational expenditures, simulations over realistic stretches of time (say 1 month). A semi-implicit temporal integration was suggested, in which the vertical direction was treated implicitly. This semi-implicit integration routine was successful,

because it permitted the larger extension of the time step when compared with the explicit method.

Via a large number of test runs the stability boundaries of the proposed numerical codes were explored by varying the time steps, mesh sizes, and numerical values for the momentum and thermal diffusivities. In so doing it was shown that with fixed meshes and fixed number of spectral polynomials the time step must fulfill the Courant–Friedrichs–Levy condition, but that in addition the diffusivities (of momentum and heat) must also be selected large enough if the errors based on the numerical approximation are to be attenuated in the course of the calculations. "Thumb rules" were proposed which give the practitioner a guideline how to select these in a physically meaningful way. Should the numerical values of the austausch coefficients needed according to these requirements be greater than physically permitted, then physically important phenomena might be damped away to such an extent that they are no longer recognizable or not as persistent as in nature. In such cases an increase of the spatial resolution and a simultaneous reduction of the values of the diffusivities might help and yield better—and stable—results.

Further results pertinent to applications in physical limnology are given in [66, 67].

ACKNOWLEDGMENTS

While performing this work Y. Wang was financially supported by the Hanns–Seidel–Stiftung and the Deutsche Forschungsgemeinschaft. K. Hutter acknowledges the support of the A. v. Humboldt Foundation and the Max Planck Society through the Max Planck Prize. A. Beckmann helped us in tracing significant literature. We thank Professor Haidvogel for allowing us to use SPEM.

REFERENCES

1. J. Adams, *MUDPACK: Multigrid software for linear elliptic partial differential equations, Version 3.0*, National Center for Atmospheric Research, Boulder, CO, 1991. [Scientific Computing Division User Doc]
2. A. Arakawa and V. R. Larm, Computational design of the basic dynamical processes of the UCLA general circulation model, *Methods Comput. Phys.* **17,** 173 (1977).
3. J. O. Backhaus and D. Hainbucher, A finite difference general circulation model for shelf seas and its application to low frequency variability on the North European Shelf, in *Three-Dimensional Models of Marine and Estuarine Dynamics*, edited by Nihoul and Jamart. Oceanography Series, Vol. 45 (Elsevier, Amsterdam, 1987), p. 221.
4. B. Barnier, P. Marchesiello, A. P. de Miranda, J.-M. Molines, and M. Coulibaly, A sigma-coordinate primitive equation model for studying the circulation in the South Atlantic. Part I. Model configuration with error estimates, *Deep-Sea Res.*, in press (1997).
5. J. M. Beckers, Application of a 3D model to the Western Mediterranean, *J. Marine Systems* **1,** 315 (1991).
6. A. Beckmann and D. B. Haidvogel, Numerical simulation of flow around a tall, isolated seamount. Part I. Problem formulation and model accuracy, *J. Phys. Oceanogr.* **23,** 1736 (1993).
7. A. Beckmann and S. Diebels, Effects of the horizontal component of the Earth's rotation on wave propagation on an f-plane. *Geophys. Astrophys. Fluid Dyn.* **76,** 95 (1994).
8. A. Beckmann and D. B. Haidvogel, A Numerical simulation of flow at Fieberling Guyot. *J. Geophys. Res.* **102,** 5595 (1997).
9. J. R. Bennett, A three-dimensional model of Lake Ontario's summer circulation, Part I: Comparison with Observations. *J. Phys. Oceanogr.* **7,** 591 (1977).
10. R. Bleck, C. Rooth, D. Hu, and L. Smith, Salinity-driven thermocline transients in a wind- and thermohaline-forced isopycnic coordinate model of the North Atlantic, *J. Phys. Oceanogr.* **22,** 1486 (1992).

11. A. F. Blumberg and G. L. Mellor, A Description of a three-dimensional coastal ocean circulation model, in Three-dimensional Coastal Ocean Models, edited by Mooers. *Coastal and Estuarine Sciences* **4,** 1 (1987).
12. D. C. Chapman and D. B. Haidvogel, Formation of Taylor caps over a tall isolated seamount in a stratified ocean. *Geophys. Astrophys. Fluid Dyn.* **64,** 31 (1992).
13. D. C. Chapman and D. B. Haidvogel, Generation of internal lee waves over a tall isolated seamount. *Geophys. Astrophys. Fluid Dyn.* **69,** 31 (1993).
14. M. D. Cox, *A Primitive Equation Three-Dimensional Model of the Ocean*, Tech. Rep. 1, GFDL Ocean Group, Princeton University, 1984.
15. G. T. Csanady, Water circulation and dispersal mechanisms, in *Lakes: Chemistry, Geology, Physics*, edited by A. Lerman (Springer-Verlag, New York/Heidelberg/Berlin, 1978).
16. G. T. Csanady, *Circulation in the Coastal Ocean* (Reidel, Dordrecht, 1984).
17. A. M. Davies, A three-dimensional numerical model of semi-diurnal tides on the European continental shelf, in *Three-Dimensional Models of Marine and Estuarine Dynamics*, edited by Nihoul and Jamart, Oceanography Series, Vol. 45 (Elsevier, Amsterdam, 1987), p. 573.
18. D. E. Dietrich, M. G. Marietta, and P. J. Roache, An ocean modelling system with turbulent boundary layers and topography: Model description, *Int. J. Numer. Methods Fluids* **7,** 833 (1987).
19. J. W. Dippner, A frontal-resolving model for the German Bight, *Continental Shelf Res.* **13**(1), 49 (1993).
20. W. Eifler and W. Schrimpf, ISPRAMIX, a hydrodynamic program for computing regional sea circulation patterns and transfer processes, *Commission of the European Communities*, EUR Report EUR 14856EN, 1992.
21. G. Z. Forristall, Three-dimensional structure of storm generated currents, *J. Geophys. Res.* **79,** 2721 (1974).
22. I. Fukumori, J. Benveniste, C. Wunsch, and D. B. Haidvogel, Assimilation of sea surface topography into an ocean circulation model using a steady-state smoother, *J. Phys. Oceanogr.* **23,** 1831 (1993).
23. D. B. Haidvogel, J. L. Wilkin, and R. Young, A semi-spectral primitive equation ocean circulation model using vertical sigma and orthogonal curvilinear horizontal coordinates, *J. Comput. Phys.* **94,** 151 (1991).
24. D. B. Haidvogel, A. Beckmann, and K. S. Hedström, Dynamical simulations of filament formation and evolution in the coastal transition zone, *J. Geophys. Res.* **96,** 15017 (1991).
25. D. B. Haidvogel, A. Beckmann, D. C. Chapman, and R.-Q. Lin, Numerical simulation of flow around a tall, isolated seamount. Part II. Resonant generation of trapped waves, *J. Phys. Oceanogr.* **23,** 2373 (1993).
26. D. B. Haidvogel and A. Beckmann, Numerical models of the coastal ocean, *The Sea*, in press (1997).
27. P. F. Hamblin and E. Hollan, On the gravitational seiches of Lake Constance and their generation, *Schweiz. Z. Hydrol.* **40**(1) (1978).
28. N. S. Heaps, Vertical structure of current in homogeneous and stratified waters, *Hydrodynamics of Lakes*, edited by K. Hutter (Springer-Verlag, Vienna/New York, 1984). [CISM-Lectures]
29. K. S. Hedström, *User's Manual for a Semi-Spectral Primitive Equation Ocean Circulation Model* (Institute for Naval Oceanography, Stennis Space Center, MS, 1990).
30. A. J. Hermann and H.-M. Hsu, A vertical coordinate mapping technique for semi-spectral primitive equation models of ocean circulation, *J. Atmos. Ocean. Tech.* **10,** 381 (1993).
31. A. J. Hermann and W. B. Owens, Energetics of gravitational adjustment for mesoscale chimneys, *J. Phys. Oceanogr.* **23,** 346 (1993).
32. E. E. Hofmann, K. S. Hedström, J. R. Moisan, D. B. Haidvogel, and D. L. Mackas, Use of simulated drifter tracks to investigate general transport patterns and residence times in the coastal transition zone, *J. Geophys. Res.* **96,** 15041 (1991).
33. E. Hollan, Strömungsmessungen im Bodensee, *Sechster Ber. AWBR* **6,** 112 (1974).
34. E. Hollan and T. J. Simons, Wind-induced changes of temperature and currents in Lake Constance, *Arch. Met. Geophys, Bioklim., Ser. A* **27,** 333 (1978).
35. K. Hutter and J. Trösch, Über die hydromechanischen und thermodynamischen Grundlagen der Seezirkulation, *Mitteilung der Versuchasanstalt für Wasserbau, Hydrologie und Glaziologie,* No. 20 (ETH, Zürich, 1975).
36. K. Hutter, G. Oman, and H. G. Ramming, Wind-bedingte Strömungen des homogenen Zürichsees. *Mitteilung der Versuchsanstalt für Wasserbau, Hydrologie und Glaziologie,* No. 61 (ETH, Zürich, 1982).

37. K. Hutter, Fundamental equations and approximations, *Hydrodynamics of Lakes*, edited by K. Hutter (Springer-Verlag, Vienna/New York, 1984). [CISM-Lectures]

38. K. Hutter, Mathematische Vorhersage von barotropen und baroklinen Prozessen im Zürich und Luganersee. *Vierteljahrschrift der Naturforschenden Gesellschaft in Zürich.* **129,** 51 (1984).

39. K. Hutter, Hydrodynamic Modelling of Lakes. *Transport Phenomena in the Environment*, Gulf Publishing Company, Houston, 897 (1986).

40. K. Hutter, Großskalige Wasserbewegung in Seen: Grundlage der physikalischen Limnologie. *Dynamik umweltrelevanter Systeme*, edited by K. Hutter (Springer-Verlag, Berlin/Heidelberg/New York, 1991).

41. K. Hutter, Waves and Oscillations in the Ocean and in Lakes. *Continuum Mechanics in Environmental Sciences and Geophysics*, edited by K. Hutter (Springer-Verlag, Berlin/Heidelberg/New York, 1993).

42. K. Hutter, G. Bauer, Y. Wang, and P. Güting, Forced response in enclosed lakes, *IUTAM Symposium on Physical Limnology, Broome, Australia, September 3–8, 1995.*

43. Internationale Gewässerschutzkomission für den Bodensee, *Internationale Bodensee-Tiefenvermessung.* Landesvermessungsamt Baden Württemberg (1990).

44. J. T. C. Ip and D. R. Lynch, *Three-Dimensional Shallow Water Hydrodynamics on Finite Elements: Nonlinear Time-Stepping Prognostic Model*, Report NML-94-1, Numerical Methods Laboratory, Dartmouth College, Hanover, NH, USA 03755, 1994.

45. M. Iskandarani, D. B. Haidvogel, and J. P. Boyd, A staggered spectral element model with applications to the oceanic shallow water equations. *International Journal of Numerical Methods in Fluids* **20,** 393 (1995).

46. A. Lehmann, Ein dreidimensionales baroklines wirbelauflösendes Modell der Ostsee. *Ber. Inst. f. Meeresk., Kiel*, No. 231, p. 104 (1992).

47. A. Lehmann, A three-dimensional baroclinic eddy resolving model of the Baltic Sea. *Tellus A* **47,** 1013 (1995).

48. M. Maiss, J. Ilmberger, and K. O. Münnich, Vertical mixing in Überlingersee (Lake Constance) traced by A SF_6 and heat. *Aquatic Sciences* **56**(4) (1994).

49. W. H. Munk, On the wind-driven ocean circulation. *J. Meteorology* **7,** 79 (1950).

50. G. Oman, Das Verhalten des geschichteten Zürichsees unter äusseren Windlasten. *Mitteilung der Versuchsanstalt für Wasserbau, Hydrologie und Glaziologie*, No. 60 (ETH Zürich, 1982).

51. F. Peeters, *Horizontale Mischung in Seen*, Dissertation (ETH, Zürich, 1994).

52. T. Pohlmann, A three dimensional circulation model of the South China Sea, in *Three-Dimensional Models of Marine and Estuarine Dynamics*, edited by Nihoul and Jamart (1987), p. 245.

53. H.-G. Ramming and Z. Kowalik, *Numerical Modelling of Marine Hydrodynamics*, Oceanography Series, Vol. 26 (Elsevier, Amsterdam, 1980), p. 1.

54. P.-T. Shaw, A numerical simulation of the evolution and propagation of gulf stream warm-core rings. *J. Phys. Oceanogr.* **24,** 573 (1994).

55. T. J. Simons, *Circulation Models of Lakes and Inland Seas*, Canadian Bulletin of Fisheries and Aquatic Sciences. Bulletin 203, Ottawa, 1980.

56. S. Serruya, E. Hollan, and B. Bitsch, Steady winter circulations in Lakes Constance and Kinneret driven by wind and main tributaries, *Arch. Hydrobiol. Suppl.* **70**(1), 32 (1984).

57. L. D. Spraggs and R. L. Street, *Three-Dimensional Simulation of Thermally-Influenced Hydrodynamic Flows.* Stanford University, Dept. of Civil Engineering, Technical Report 190, 1975.

58. Y. Song and D. B. Haidvogel, A semi-implicit ocean circulation model using a generalized topography-following coordinate. *J. Comput. Phys.* **115,** 228 (1994).

59. J. Sündermann, Die hydrodynamisch-numerische Berechnung der Vertikalstruktur von Bewegungsvorgängen in Kanälen und Becken, *Mitt. Inst. Meereskunde Univ. Hamburg* **19** (1971).

60. K.-T. Tee, Simple models to simulate three-dimensional tidal and residual cuurents, in Three-dimensional Coastal Ocean Models, edited by Mooers, *Coastal and Estuarine Sciences* **4,** 125 (1987).

61. J. Trösch, Strömung in Seen—Dreidimensionale Simulation mit finiten Elementen. *Mitteilung der Versuchsanstalt für Wasserbau, Hydrologie und Glaziologie*, No. 63 (ETH Zürich, 1983).

62. S. J. Walker, *A 3-Dimensional Non-Linear Variable Density Hydrodynamic Model with Curvilinear Coordinates*, Tech. Rep. OMR-60/00, CSIRO Division of Oceanography (in preparation, 1995).

63. J. Wang, L. A. Mysak, and R. G. Ingram, A three-dimensional numerical simulation of Hudson Bay summer ocean circulation: topographic gyres, separations and coastal jets. *J. Phys. Oceangr.* **24,** 2496 (1994).
64. Y. Wang, *Windgetriebene Strömungen in einem Rechteckbecken und im Bodensee*, Shaker Verlag, Aachen (1996). Dissertation, Department of Mechanics, Technische Hochschule Darmstadt.
65. Y. Wang and K. Hutter, Three-dimensional wind-induced circulation in homogeneous lakes (in preparation, 1996).
66. Y. Wang and K. Hutter, Three-dimensional wind-induced baroclinic circulation in a rectangle. A numerical treatment by a spectral model (in preparation, 1996).
67. Y. Wang, K. Hutter, and E. Bäuerle, Three-dimensional wind-induced baroclinic circulation in Lake Constance (in preparation, 1996).
68. Y. Wang and K. Hutter, ADI methods applied to a semi-spectral code of the shallow water equations (in preparation, 1997).
69. J. L. Wilkin and D. C. Chapman, Scattering of coastal-trapped waves by irregularities in coast-line and topography. *J. Phys. Oceanogr.* **20,** 396 (1990).
70. J. L. Wilkin and K. S. Hedström, *User's Manual for Orthogonal Curvilinear Grid-Generation Package.* CSIRO (Hobart, Tasmania, Australia, 1991).
71. J. L. Wilkin, J. Mansbridge, and K. S. Hedström, An application of the capacitance matrix method to accomodate masked land areas and island circulations in a primitive equation ocean model. *Int. J. Num. Meth. Fl.* **20,** 649 (1991).